

Intelligent Reconfigurable Reflecting Surfaces for Free Space Optical Communications

Marzieh Najafi, *Student Member, IEEE*, Bernhard Schmauss,
and Robert Schober, *Fellow, IEEE*

Abstract

In this paper, we investigate the use of intelligent reflecting surfaces (IRSs) to relax the line-of-sight requirement of free space optical (FSO) systems. Considering a Gaussian laser beam, we first design a phase shift distribution across the IRS that enables the reflection of the incident beam in any desired direction, i.e., realizing the generalized Snell's law. Moreover, for the designed phase-shift profile, we show that there exists an equivalent mirror-assisted FSO system that generates a reflected electric field on a mirror that is identical to that on the IRS in the original system. However, the location of the laser source and the properties of the emitted Gaussian laser beam are different in the original and the equivalent systems. This equivalence allows us to study the mirror-assisted system, employing the imaging technique from geometric optics, instead of directly analyzing the original IRS-assisted system. Based on this analysis, we model the geometric and misalignment losses (GML) and characterize the impact of the physical parameters of the IRS, such as its size, position, and orientation, on the end-to-end FSO channel. Moreover, we develop a statistical model for the GML which accounts for the random movements of IRS, transmitter (Tx), and receiver (Rx) due to building sway. Furthermore, we analyze the outage probability of an IRS-assisted FSO link based on the derived channel model. Our simulation results validate the accuracy of the developed channel model and offer various insights for system design. For instance, both our simulations and theoretical analysis reveal that even if the variances of the fluctuations of the Tx, IRS, and Rx positions caused by building sway are identical, their impact on the end-to-end channel is not necessarily the same and depends on the relative positioning of these three nodes.

I. INTRODUCTION

Optical wireless systems, e.g., free space optical (FSO) systems, are promising candidates to meet the high data rate requirements of the next generation of wireless communication networks and beyond [2]–[5]. FSO systems offer the large bandwidth needed for high rate applications such as wireless backhauling, while the corresponding transceivers are relatively cheap compared to their radio frequency

Marzieh Najafi and Robert Schober are with the Institute for Digital Communications, Friedrich-Alexander-University Erlangen-Nuremberg (FAU), Germany (email: {marzieh.najafi and robert.schober}@fau.de).

Bernhard Schmauss is with the Institute for Microwaves and Photonics, Friedrich-Alexander-University Erlangen-Nuremberg (FAU), Germany (email: bernhard.schmauss@fau.de).

This paper was presented in part at IEEE Globecom 2019 [1].

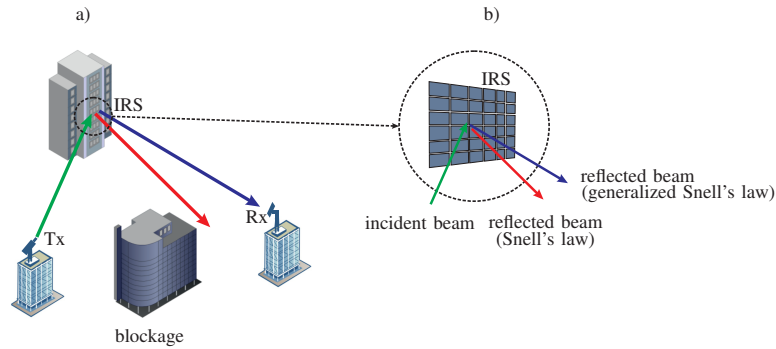


Fig. 1. a) IRSs can be deployed to relax the LOS requirement between Tx and Rx in FSO systems. b) IRS can reflect the beam in a desired direction.

(RF) counterparts and easy to implement. However, FSO systems require a line-of-sight (LOS) link between the transmitter (Tx) and receiver (Rx) and are impaired by atmospheric turbulence induced fading, large atmospheric losses in dense fog and heavy snowfall, and geometric and misalignment losses (GML) [2]. To overcome these impairments, various techniques have been proposed in the literature to improve the reliability of FSO systems, including aperture averaging [6], diversity techniques [4], [5], adaptive optics [7], and RF links as backup for FSO links [8], [9]. Nevertheless, the requirement of an LOS link still remains a severe limitation for the applicability of FSO systems. In the absence of an LOS link, a viable solution is to deploy a relay node that has an LOS to both Tx and Rx [10], [11]. However, such a relay node has to be equipped with a partial or complete FSO transceiver chain. For example, a decode-and-forward relay node requires a laser source (LS), lens, photo-detector (PD), tracking system, and signal processing units, which significantly increases the system complexity. To avoid this drawback, in this paper, we propose to employ reconfigurable optical intelligent reflecting surfaces (IRSs) to relax the LOS requirement constraint for FSO systems. Unlike relays, IRSs are energy- and cost-efficient since they are composed of passive elements and can be installed on existing infrastructure, e.g., building walls, cf. Fig. 1 a).

IRSs are planar arrays of resonant sub-wavelength artificial structures which enable reflection of the incident beam in a desired direction by manipulating the wavefront by changing the phase of the beam over the surface of the IRS. This results in the generalized Snell's law of reflection [12]–[14], cf. Fig. 1 b). In fact, IRSs belong to the larger category of metasurfaces which are able to change the properties of an impinging electromagnetic wave including its amplitude, phase, dispersion, momentum, and polarization [15]. Moreover, they can be classified into two categories, namely reconfigurable and non-reconfigurable surfaces, depending on whether or not the configuration of the surface can be changed post fabrication. The refractive index of reconfigurable optical metasurfaces and in turn the phase of the light can be changed e.g., by applying an electrical voltage to the surface [16]. The

design, fabrication, and analysis of optical metasurfaces have been an active area of research in the nanotechnology, material science, and physics literature, see review papers [17]–[20]. For instance, in [16], an electrically-reconfigurable optical metasurface was designed and fabricated based on gate-tunable conducting oxide materials. Moreover, the authors of [21] proposed to employ optical metasurfaces for inter/intra chip communications. Furthermore, in [22], an optical IRS was designed and experimentally tested to establish a non-LOS optical wireless link in an indoor application. In this paper, we focus on reconfigurable IRSs and study an IRS enabled FSO link between a Tx and an Rx. In the following, we summarize the main contributions of this paper.

- Considering a Gaussian laser beam, we first specify the phase shift distribution across the IRS that enables the reflection of the incident beam in a desired direction. For this phase-shift profile, we show that there exists an equivalent mirror-assisted FSO system that generates a reflected electric field on the mirror that is identical to that on the IRS in the original system. However, the location of the laser source and the properties of the emitted Gaussian laser beam are different in the original and the equivalent systems. This equivalence allows us to study the mirror-assisted system, exploiting the imaging technique from geometric optics, instead of directly analyzing the original IRS-assisted system.
- We characterize the end-to-end FSO channel as a function of the area, position, and orientation of the IRS by deriving the GML of the end-to-end link, i.e., the Tx-to-IRS-to-Rx link, which we refer to as conditional GML.
- In an IRS-assisted FSO link not only the Tx and Rx may be subjected to random movements caused by building sway, but also the IRS. Therefore, we develop a statistical channel model which accounts for the impact of building sway on all three nodes. In particular, we develop statistical channel models for both two-dimensional (2D) and three-dimensional (3D) systems. In fact, since deriving the channel model for 2D systems is more straightforward and provides more insights, we first develop a 2D model. Then, based on the insights gained from the 2D channel model, we develop a channel model for practical 3D systems.
- We analyze the system performance in terms of the outage probability. Thereby, we account for both the GML and the atmospheric turbulence induced fading. For the former, we adopt the statistical model developed in this paper, and for the latter, we consider both log-normal (LN) and Gamma-Gamma (GG) atmospheric turbulence induced fading to account for weak and moderate-to-strong turbulences [3], respectively.
- Simulations are used to validate our derivations and to illustrate the impact of the system parameters such as the variance of the fluctuations induced by building sway and the beamwidth on system

performance. For example, our results reveal that for a given end-to-end distance, when the building sway of either the Tx or IRS is more severe than that of the Rx, placing the IRS approximately in the middle between the Tx and Rx minimizes the outage probability. However, when the building sway of the Rx is more severe, moving the IRS closer to the Rx leads to a smaller outage probability.

To the best of the authors' knowledge, the communication-theoretical analysis of an IRS-assisted FSO link, including corresponding conditional and statistical GML models, have been first considered in [1], which is the conference version of this paper. In contrast to [1], which studied mechanically tunable IRSs, in this paper, we consider electronically tunable IRSs, which can provide a desired angle of reflection without mechanical movement, and derive the corresponding conditional and statistical GML models of the resulting IRS-assisted FSO link. Moreover, unlike this paper, an outage analysis was not included in [1]. Furthermore, the recent works [23], [24] proposed to employ optical IRSs for visible light communications (VLCs). However, the analyses in our paper are fundamentally different from those in [23], [24] due to the inherent differences between FSO and VLC systems. For example, FSO systems employ narrow laser beams whereas VLC systems use non-directional light-emitting diodes.

The remainder of this paper is organized as follows. The system and channel models are presented in Section II. The conditional GML model and the corresponding statistical channel model are derived in Sections III and IV, respectively, for a 2D system. These models are then extended to a practical 3D system in Section V. The outage probability of an IRS-assisted FSO link is analyzed in Section VI. Simulation results are presented in Section VII, and conclusions are drawn in Section VIII.

Notations: Boldface lower-case and upper-case letters denote vectors and matrices, respectively. \mathbb{R}^+ and \mathbb{R} represent the sets of positive real and real numbers, respectively. Superscript $(\cdot)^T$ and $\mathbb{E}\{\cdot\}$ denote the transpose and expectation operators, respectively, and $\|\mathbf{a}\|$ is the Euclidean norm of vector \mathbf{a} . Moreover, $\ln(x)$, $\text{erf}(x)$, $I_0(x)$, $K_\nu(x)$, ${}_pF_q(a_1, \dots, a_l; b_1, \dots, b_q; z)$, and $\Gamma(x)$ represent the natural logarithm, the Gaussian error function, the zero-order modified Bessel function of the first kind, the ν -th order modified Bessel function of the second kind, the hypergeometric function, and the Gamma function, respectively. Furthermore, \mathbf{I}_N is the $N \times N$ identity matrix, $\text{diag}\{a_1, \dots, a_n\}$ is a diagonal matrix with a_i , $i = 1, \dots, n$, as main diagonal entries, and $\mathbf{a} \cdot \mathbf{b}$ denotes the inner product of vectors \mathbf{a} and \mathbf{b} . Finally, $\mathbf{R}_\tau = \begin{bmatrix} \cos \tau & -\sin \tau \\ \sin \tau & \cos \tau \end{bmatrix}$ denotes a counter-clockwise rotation matrix with rotation angle τ and $\mathbf{T}_\tau = \text{diag}\{\cos \tau, 1\}$ is a transformation matrix.

II. SYSTEM AND CHANNEL MODELS

In this section, we first present the system model. Then, we introduce the Gaussian laser beam and the considered FSO channel model.

A. System Model

We consider an FSO communication system comprising a Tx equipped with an LS emitting a Gaussian beam, an IRS, and an Rx equipped with a lens and a PD. We assume that the LOS between the Tx and the Rx is blocked, and hence, the communication between them is enabled by an IRS which has a LOS to both the Tx and the Rx, cf. Fig. 1. The aperture of the LS is directed towards the IRS; the IRS reflects the optical beam that it receives towards the lens of the Rx; and the lens focuses the beam to the PD to collect the optical energy. As is customary for the analysis of optical systems [25], we first consider a 2D system model. The impact of the position, orientation, and building sway on the GML can be conveniently analyzed for the 2D system model, cf. Sections III and IV, and then generalized to a 3D system, cf. Section V. In the following, we define the position and orientation of the LS, the IRS, and the lens for both the 2D and 3D system models, cf. Fig. 2.

1) *2D System Model*: We consider the yz -coordinate system and assume that the LS is located at point (y_{ls}, z_{ls}) and the centers of the IRS and the Rx lens are located at points $(y_r, 0)$ and (y_l, z_l) , respectively. Moreover, without loss of generality, we assume that the IRS lies on the y axis and define the origin as the intersection of the beam line¹ and the IRS line, see Fig. 2a). The lengths of the IRS line and the lens line are denoted by $2a_r$ and $2a_l$, respectively. Moreover, θ_i and θ_r denote the angles of incident and reflection at the IRS, respectively, see Fig. 2a). Note that unlike normal mirrors, for IRSs, θ_i and θ_r are not necessarily identical [12], [13], see also Sections III and V. Finally, let $\theta_{r,l}$ denote the angle between the reflected beam and the normal vector of the lens.

2) *3D System Model*: We assume that the LS is placed at point (x_{ls}, y_{ls}, z_{ls}) , the IRS lies in the $x - y$ plane and its center is at point $(x_r, y_r, 0)$, and the lens is a circle with radius a_l centered at point (x_l, y_l, z_l) . Similar to the 2D system model, we define the beam footprint center on the IRS as the origin. Let $\Psi_i = (\theta_i, \phi_i)$ and $\Psi_r = (\theta_r, \phi_r)$ represent the angles of incident and reflection at the IRS, respectively, where θ_m , $m \in \{i, r\}$, denotes the elevation angle (i.e., the angle between the beam line and the z axis) and ϕ_m , $m \in \{i, r\}$, is the azimuth angle (i.e., the angle between the projection of the beam line on the $x - y$ plane and the x axis), see Fig. 2b). Without loss of generality, we define the x

¹The beam line is the line that connects the laser source with the center of the beam footprint.

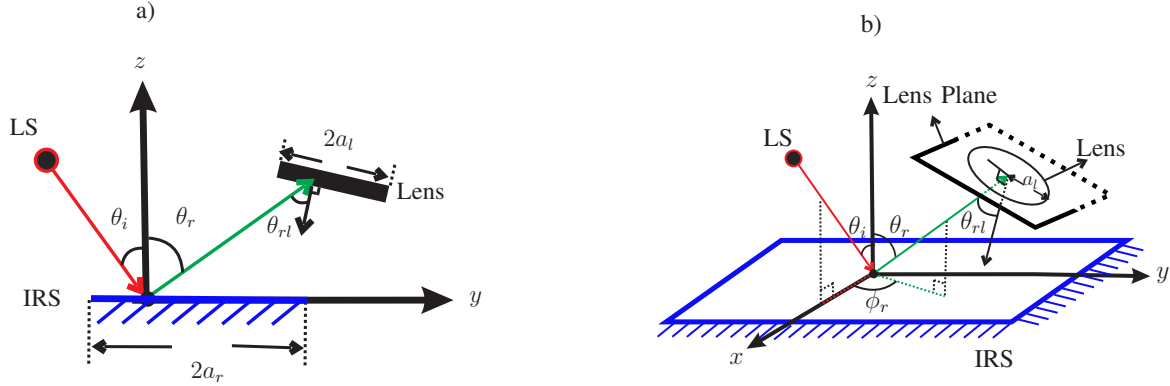


Fig. 2. Schematic illustration of the considered IRS-assisted FSO system for a) 2D and b) 3D systems.

and y axes such that $\phi_i = 0$ holds. To characterize the orientation of the lens, we use the angle between the reflected beam and the normal vector of the lens and denote it by θ_{rl} .

B. Gaussian Beam

For convenience of notation, for presenting the electric field of a Gaussian beam, we define new $\hat{y}\hat{z}$ -2D and $\hat{x}\hat{y}\hat{z}$ -3D Cartesian coordinate systems, which have the LS located at the origin. A Gaussian beam propagating in $+\hat{z}$ direction has the following electric field [26]

$$E(a, \hat{z}) = E_0 \left(\frac{w_0}{w(\hat{z}, w_0)} \right)^{\frac{n-1}{2}} \exp \left(\frac{-a^2}{w^2(\hat{z}, w_0)} \right) \exp(j\phi_G(a, \hat{z}, w_0)) \quad \text{with phase} \quad (1)$$

$$\phi_G(a, \hat{z}, w_0) = -k\hat{z} - k \frac{a^2}{2R(\hat{z}, w_0)} + \psi(\hat{z}, w_0), \quad (2)$$

where n denotes the dimension of the space, i.e., $n = 2$ and $n = 3$ for the 2D and 3D spaces, respectively, and a denotes the radial distance from the beam line, which is given by $a = |\hat{y}|$ and $a = \sqrt{\hat{x}^2 + \hat{y}^2}$ for 2D and 3D systems, respectively. Moreover, E_0 denotes the electric field at the origin, w_0 denotes the beam waist radius, $k = \frac{2\pi}{\lambda}$ is the wave number, and λ is the optical wavelength. Furthermore, $R(\hat{z}, w_0) = \hat{z} \left(1 + \left(\frac{z_R}{\hat{z}} \right)^2 \right)$ is the curvature radius of the beam's wavefront at distance \hat{z} , $z_R = \frac{\pi w_0^2}{\lambda}$, $\psi(\hat{z}, w_0) = \frac{n-1}{2} \tan^{-1} \left(\frac{\hat{z}}{z_R} \right)$, and $w(\hat{z}, w_0)$ is the beamwidth at distance \hat{z} given by

$$w(\hat{z}, w_0) = w_0 \sqrt{1 + \left(\frac{\hat{z}}{z_R} \right)^2}. \quad (3)$$

The power density of the Gaussian beam in (1) at any point on a line/plane perpendicular to the propagation direction at distance a from the center of the beam footprint is given by [2], [3]

$$I_G^{\text{orth}}(a|\hat{z}, w_0) = I_G^{\text{max}}(\hat{z}, w_0) \exp \left(-\frac{2a^2}{w^2(\hat{z}, w_0)} \right), \quad (4)$$

where $I_G^{\max}(\hat{z}, w_0) = \frac{\sqrt{2}}{\sqrt{\pi w(\hat{z}, w_0)}}$ and $I_G^{\max}(\hat{z}, w_0) = \frac{2}{\pi w^2(\hat{z}, w_0)}$ for the 2D and 3D spaces, respectively. Note that $I_G^{\max}(\hat{z}, w_0)$ is a normalization constant that ensures that for any given \hat{z} , the integral of $I_G^{\text{orth}}(a|\hat{z}, w_0)$ over \hat{y} and (\hat{x}, \hat{y}) for 2D and 3D systems, respectively, is equal to 1.

C. Channel Model

We assume an intensity modulation/direct detection (IM/DD) FSO system, where the PD measures the received optical signal power [2]. Moreover, we assume that background noise is the dominant noise source at the PD and therefore the noise is independent from the signal [2]. The received signal at the PD of the Rx, denoted by y_s , is given by

$$y_s = hx_s + n, \quad (5)$$

where $x_s \in \mathbb{R}^+$ is the transmitted optical symbol (intensity), $n \in \mathbb{R}$ is zero-mean real-valued additive white Gaussian shot noise with variance σ_n^2 caused by the ambient light at the PD, and $h \in \mathbb{R}^+$ denotes the end-to-end FSO channel gain from the Tx to the Rx. Moreover, we assume an average power constraint $\mathbb{E}\{x_s\} \leq P$.

The FSO channel gain, h , is affected by several phenomena and can be modeled as follows [3]

$$h = \eta h_p h_a h_g, \quad (6)$$

where η is the responsivity of the PD and h_p , h_a , and h_g represent the atmospheric loss, atmospheric turbulence induced fading, and GML, respectively. In particular, the atmospheric loss, h_p , is deterministic and represents the power loss over a propagation path due to absorption and scattering of the light by particles in the atmosphere [2]. The atmospheric turbulence, h_a , is a random variable (RV) and induced by inhomogeneities in the temperature and the pressure of the atmosphere. It is typically modeled as LN and GG distributed RV for weak and moderate-to-strong turbulence conditions, respectively [3]. The GML, h_g , is caused by the divergence of the optical beam along the propagation distance as well as the misalignment between the laser beam line and the center of the Rx lens due to building sway [2], [8]. Our goal is to mathematically determine the impact of the IRS on the quality of the FSO channel. More specifically, the impact of the IRS on the end-to-end FSO channel is reflected in h_p and h_g as discussed in the following:

i) Quality of reflection: In addition to reflection, practical IRSs may also absorb or scatter some fraction of the beam power. Let ζ denote the reflection efficiency, i.e., the fraction of power reflected by the IRS, which depends on the operating frequency as well as the bias voltage applied to the surface.

For FSO systems with $\lambda = 1550$ nm, values in the range $[0.7, 1]$ are typical [16], [27]. The absorption at the IRS can be regarded as a part of the atmospheric loss h_p . In particular, h_p is modeled as [8]

$$h_p = \zeta 10^{-\kappa d_{e2e}/10}, \quad (7)$$

where κ denotes the weather-dependent attenuation coefficient of the FSO link and d_{e2e} is the end-to-end distance that the optical beam travels from the Tx to the Rx, i.e., $d_{e2e} = d_{sr} + d_{rl}$, where d_{sr} and d_{rl} denote the distances from the LS to the IRS and from the IRS to the Rx, respectively.

ii) Relative position, orientation, and size of IRS: The relative position and orientation of the IRS with respect to (w.r.t.) the laser beam determines the distribution of the *reflected* optical power in space. Moreover, the size of the IRS determines which part of the lens is covered by the reflected beam. These parameters affect the *mean* of the GML h_g .

iii) Building Sway: Tx, IRS, and Rx are affected by the random movements of the buildings that they are installed on. This further increases the beam misalignment and affects the *statistics* of the GML h_g , i.e., building sway causes h_g to be random.

Based on the above discussion, quantifying the impact of the IRS on the end-to-end FSO channel reduces to characterizing the corresponding GML h_g . To this end, we develop both a conditional model that accounts for the position, orientation, and size of the IRS and a statistical model that accounts for the random fluctuations of the IRS's position due to building sway. We first derive the conditional and statistical GML models for 2D systems in the following two sections, and then generalize these models to practical 3D systems in Section V exploiting the insights gained from the 2D analysis.

III. CONDITIONAL GML - 2D SYSTEM

In this section, first, we find the power distribution of the emitted Gaussian beam across the IRS. Then, we investigate how the IRS changes the direction of the reflected beam, and finally, we determine the conditional GML for given positions and orientations of the LS, the IRS, and the Rx lens.

A. Power Distribution Across IRS

Let $I_G^{\text{irs}}(y|d_{sr}, \theta_i, w_0)$ denote the power distribution across the IRS at point $(y, 0)$ which is a function of the position of the LS, specified by d_{sr} and θ_i , and the beam waist radius w_0 . The following lemma provides the power distribution across the IRS.

Lemma 1: The power distribution of a Gaussian beam originating from the LS across the IRS is obtained as

$$I_G^{\text{irs}}(y|d_{sr}, \theta_i, w_0) = I_G^{\text{orth}}(y|d_{sr}, \tilde{w}_0), \quad (8)$$

where \tilde{w}_0 is the solution of equation $w(d_{sr}, \tilde{w}_0) = \frac{w(d_{sr}, w_0)}{\cos \theta_i}$ and is given by

$$\tilde{w}_0 = \frac{1}{2} \left[\frac{w_0^2}{\cos^2 \theta_i} + \frac{\lambda^2 d_{sr}^2}{\pi^2 \cos^2 \theta_i w_0^2} + \left(\left(\frac{w_0^2}{\cos^2 \theta_i} + \frac{\lambda^2 d_{sr}^2}{\pi^2 \cos^2 \theta_i w_0^2} \right)^2 - 4 \frac{\lambda^2 d_{sr}^2}{\pi^2} \right)^{\frac{1}{2}} \right]^{\frac{1}{2}}. \quad (9)$$

Proof: Please refer to Appendix A. ■

Lemma 1 states that the power distribution for a non-orthogonal beam impinging on the IRS is equivalent to that of an orthogonal beam originating from a source with the same distance to the IRS, d_{sr} , but with a different beam waist radius, \tilde{w}_0 . Moreover, the width of the orthogonal beam at distance d_{sr} is obtained as $w(d_{sr}, \tilde{w}_0) = \frac{w(d_{sr}, w_0)}{\cos(\theta_i)}$. Next, we present a useful corollary of Lemma 1.

Corollary 1: Let us consider a new LS whose location is specified by $\hat{\theta}_i$ and d_{sr} and which emits a Gaussian beam with waist radius \hat{w}_0 . For any *arbitrary* $\hat{\theta}_i$, the power distribution across the IRS caused by the new LS becomes identical to that created by the original LS, i.e.,

$$I_G^{\text{irs}}(y|d_{sr}, \hat{\theta}_i, \hat{w}_0) = I_G^{\text{irs}}(y|d_{sr}, \theta_i, w_0), \quad (10)$$

if \hat{w}_0 is chosen as the solution to equation $w(d_{sr}, \hat{w}_0) = \frac{\cos \hat{\theta}_i}{\cos \theta_i} w(d_{sr}, w_0)$ which is given in closed form by (9) after substituting $\cos \theta_i$ by $\frac{\cos \hat{\theta}_i}{\cos \theta_i}$.

Proof: According to Lemma 1, for the LS, $I_G^{\text{irs}}(y|d_{sr}, \theta_i, w_0) = I_G^{\text{orth}}(y|d_{sr}, \tilde{w}_0)$ holds, where \tilde{w}_0 is obtained from $w(d_{sr}, \tilde{w}_0) = \frac{w(d_{sr}, w_0)}{\cos \theta_i}$. Similarly, for the new LS, $I_G^{\text{irs}}(y|d_{sr}, \hat{\theta}_i, \hat{w}_0) = I_G^{\text{orth}}(y|d_{sr}, \tilde{\tilde{w}}_0)$ holds, where $\tilde{\tilde{w}}_0$ is obtained from $w(d_{sr}, \tilde{\tilde{w}}_0) = \frac{w(d_{sr}, \hat{w}_0)}{\cos \hat{\theta}_i}$. Therefore, $I_G^{\text{irs}}(y|d_{sr}, \theta_i, w_0) = I_G^{\text{irs}}(y|d_{sr}, \hat{\theta}_i, \hat{w}_0)$ holds when $\tilde{w}_0 = \tilde{\tilde{w}}_0$ is satisfied. This leads to $\frac{w(d_{sr}, \tilde{w}_0)}{\cos \theta_i} = \frac{w(d_{sr}, \hat{w}_0)}{\cos \hat{\theta}_i}$, which completes the proof. ■

We use the above corollary in the following subsections to specify a phase-shift profile on the IRS that not only realizes the generalized Snell's law but also allows us to derive the power distribution of the reflected beam using geometric optics.

B. Phase-shift Profile Across IRS

Given the positions of the LS, the IRS, and the lens as well as the properties of the emitted Gaussian beam, we aim to design a phase-shift profile across the IRS, denoted by $\Delta\phi(y|\theta_i, \theta_r, w_0)$, such that it causes the desired angle of reflection θ_r . To this end, we define an equivalent mirror-assisted system, which is useful for the design of $\Delta\phi(y|\theta_i, \theta_r, w_0)$.

Proposed Equivalent Mirror-assisted System: The equivalent system is constructed as follows: *i)* The IRS is replaced by a mirror. *ii)* The LS is replaced by a new LS, denoted by LS_n , which is located in a different position such that it has distance d_{sr} from the mirror and its beam hits the mirror with incident angle θ_r . Therefore, from geometric optics, the angle of reflection at the mirror is θ_r . *iii)* The LS_n emits

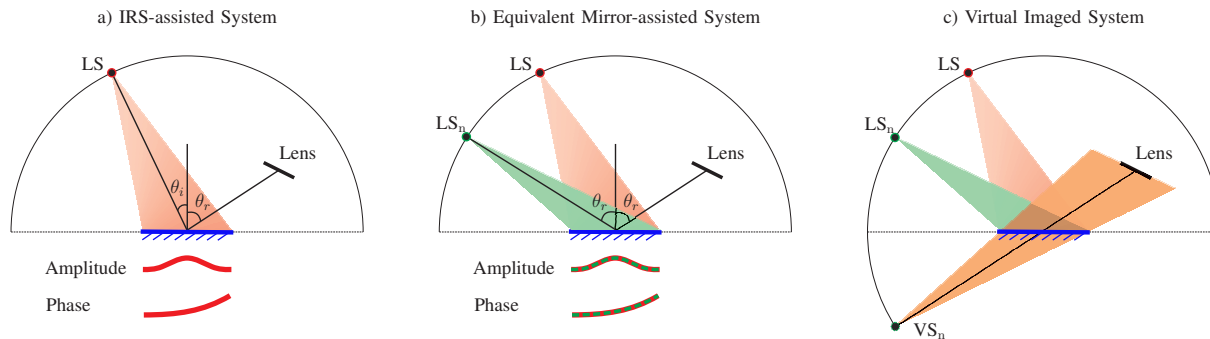


Fig. 3. Schematic illustration of the proposed equivalent mirror-assisted system. a) Original IRS-assisted system with $\theta_i \neq \theta_r$ and the corresponding amplitude and phase distribution of the reflected beam across the IRS. b) Equivalent mirror-assisted system with $\theta_i = \theta_r$ yielding the same amplitude and phase distribution of the reflected beam across the mirror as those across the IRS in the original system. c) Virtual imaged system.

a Gaussian beam with waist radius \hat{w}_0 given in Corollary 1. Thereby, according to Corollary 1, the power distributions across the mirror and the IRS in both systems are identical.

Rationale Behind the Proposed Phase-shift Design: The location of LS_n and the properties of its emitted beam (i.e., \hat{w}_0) determine the phase distribution of the wave reflected from the mirror. Now, we design the phase-shift profile, $\Delta\phi(y|\theta_i, \theta_r, w_0)$, across the IRS such that the phases of the reflected waves in both systems are also the same. This leads to the same reflected electric fields in both systems. Therefore, the angle of reflection in both systems is also identical and is given by θ_r , cf. Figs. 3a), b).

Proposed Phase-shift Profile: Considering the above discussion, we propose the following phase-shift profile across the IRS to reflect a beam with incident angle θ_i into direction θ_r .

$$\begin{aligned} \Delta\phi(y|\theta_i, \theta_r, w_0) &= \pi + \phi_G(y \cos \theta_r, d_{sr} + y \sin \theta_r, \hat{w}_0) - \phi_G(y \cos \theta_i, d_{sr} + y \sin \theta_i, w_0) \\ &\stackrel{(a)}{=} \pi + ky [\sin \theta_i - \sin \theta_r], \end{aligned} \quad (11)$$

where equality (a) holds in the far field, i.e., $d_{sr} \gg \frac{\pi w_0^2}{\lambda}$, and $\phi_G(\cdot, \cdot, \cdot)$ is given in (2).

We note that the proposed phase-shift profile in (11) is conceptually similar to the well-known constant phase-gradient-based design proposed in the literature to realize the generalized Snell's law of reflection for plane waves [12], [28], [29]. However, in this paper, we consider the Gaussian beam in (1) which, unlike plane waves, creates a non-uniform power distribution (and in general a non-linear phase distribution) across the IRS, see Fig 3a). To realize the phase-shift profile in (11), the phase shift introduced by each point on the surface can be related to the corresponding refractive index. For instance, for the IRS design proposed in [16], a desired phase shift is realized by applying an electrical voltage to the surface that locally changes the refractive index. The phase-shift profile in (11) not only realizes the generalized Snell's law but also enables us to analyze the reflected wave using the equivalent mirror-assisted system.

Remark 1: For the special case where $\theta_r = \theta_i$, $\Delta\phi(y|\theta_i, \theta_r, w_0) = \pi$ holds. This corresponds to the π -phase change that normal mirrors introduce to the reflected beam [30]. In other words, for $\theta_r = \theta_i$, the IRS reduces to a simple mirror.

C. Spatial Distribution of the Reflected Power Density

As discussed above, the reflected beams in the IRS- and mirror-assisted systems are identical. Therefore, to find the spatial power distribution of the reflected beam, we use the mirror-assisted system in Fig 3b). It is well known from geometric optics that the system in Fig. 3b) with LS_n and an infinite-size mirror can be transformed to an equivalent system with a virtual LS, denoted by VS_n , without the mirror [30], see Fig. 3c). Thereby, VS_n is the image of LS_n w.r.t. the mirror. For a mirror of finite size, the lines connecting VS_n and the boundaries of the mirror create a truncation region, denoted by \mathcal{R} , outside of which the reflected optical power is negligible. The location of VS_n is obtained as $\mathbf{p}_{vs_n} = (y_{vs_n}, z_{vs_n})^T = (y_{ls_n}, -z_{ls_n})^T = (-d_{sr} \sin \theta_r, -d_{sr} \cos \theta_r)^T$, where (y_{ls_n}, z_{ls_n}) is the location of LS_n . Using these notations, the truncation region can be formally characterized as $\mathcal{R} = \{(y, z)^T | s_1(y - y_{vs_n}) + z_{vs_n} \leq z \leq s_2(y - y_{vs_n}) + z_{vs_n}\}$, where $s_1 = \frac{-z_{vs_n}}{y_r + a_r - y_{vs_n}}$ and $s_2 = \frac{-z_{vs_n}}{y_r - a_r - y_{vs_n}}$. Moreover, let $\mathbf{p}_c = (y_c, z_c)^T$ denote the center of the beam footprint on the lens, where $y_c = \frac{\tan(\theta_r - \theta_{ri})y_l + z_l}{\tan(\theta_r - \theta_{ri}) + \cot \theta_r}$ and $z_c = \cot \theta_r y_c$. Based on the above discussion, the power density of the beam reflected by the IRS is formally given in the following lemma.

Lemma 2: Let $\hat{\mathbf{p}} = (\hat{y}, \hat{z})^T \in \mathcal{R}$ be a point on a line that is perpendicular to the reflected beam line and passes through \mathbf{p}_c , cf. Fig. 4. Assuming the phase-shift profile proposed in (11), the power density of the beam reflected from the IRS at point $\hat{\mathbf{p}}$ is given by

$$I_{\text{rff}}^{\text{orth}}(\hat{r}|d_{e2e}, \hat{w}_0) = \frac{\sqrt{2}}{\sqrt{\pi}w(d_{e2e}, \hat{w}_0)} \exp\left(-\frac{2\hat{r}^2}{w^2(d_{e2e}, \hat{w}_0)}\right), \quad (12)$$

where $\hat{r} = \|\hat{\mathbf{p}} - \mathbf{p}_c\|$ and $d_{e2e} = \|\mathbf{p}_{vs_n} - \mathbf{p}_c\|$.

Proof: The reflected beam in the IRS-assisted system is identical to that in the mirror-assisted system (given in Corollary 1) which leads to (12). ■

Lemma 2 states that the beam reflected by the IRS is a *truncated* Gaussian beam, whose width depends on the angles of incident and reflection and which originates from VS_n and is confined to area \mathcal{R} . Moreover, the size of \mathcal{R} depends on the size of the IRS as well as on its relative orientation w.r.t. the laser beam. Note that $I_{\text{rff}}^{\text{orth}}(\hat{r}|d_{e2e}, \hat{w}_0)$ attains its maximum, i.e., $\frac{\sqrt{2}}{\sqrt{\pi}w(d_{e2e}, \hat{w}_0)}$, at $\hat{r} = 0$, i.e., at the center of its footprint \mathbf{p}_c , cf. (12). Therefore, for an efficient design, we should choose θ_r such that \mathbf{p}_c

lies in the center of the lens (y_l, z_l) . This leads to an optimal θ_r^* given by

$$\tan \theta_r^* = \frac{y_l}{z_l}. \quad (13)$$

D. Conditional GML

We assume that the Rx lens focuses all optical power of the part of the beam that strikes it on the PD. Therefore, in order to compute the fraction of power collected by the PD (i.e., the conditional GML), we have to calculate the fraction of power that flows into the lens. The following proposition provides a closed-form expression for the conditional GML h_g . Let r_c denote the distance between the center of the lens and the beam line.

Proposition 1: Under the mild condition $a_l, r_c \ll d_{e2e}$, the conditional GML is given by

$$h_g = \frac{1}{2} \begin{cases} \operatorname{erf}\left(\frac{\sqrt{2} \cos \theta_{rl} \rho_1}{w(d_{e2e}, \hat{w}_0)}\right) + \operatorname{erf}\left(\frac{\sqrt{2} \cos \theta_{rl} \rho_2}{w(d_{e2e}, \hat{w}_0)}\right), & \text{if } \rho_{12} = 2a_l \\ \left| \operatorname{erf}\left(\frac{\sqrt{2} \cos \theta_{rl} \rho_1}{w(d_{e2e}, \hat{w}_0)}\right) - \operatorname{erf}\left(\frac{\sqrt{2} \cos \theta_{rl} \rho_2}{w(d_{e2e}, \hat{w}_0)}\right) \right|, & \text{otherwise,} \end{cases} \quad (14)$$

where the term $\cos \theta_{rl} \in [0, 1]$ accounts for the non-orthogonality of the lens w.r.t. the beam line². Moreover, $\rho_1 = \|\mathbf{p}_c - \hat{\mathbf{p}}_1\|$, $\rho_2 = \|\mathbf{p}_c - \hat{\mathbf{p}}_2\|$, $\rho_{12} = \|\mathbf{p}_c - \mathbf{p}_1\| + \|\mathbf{p}_c - \mathbf{p}_2\|$, where $\mathbf{p}_1 = (y_l + a_l \cos \tilde{\theta}, z_l - a_l \sin \tilde{\theta})^\top$ and $\mathbf{p}_2 = (y_l - a_l \cos \tilde{\theta}, z_l + a_l \sin \tilde{\theta})^\top$ are the corner points of the lens and $\hat{\mathbf{p}}_1$ and $\hat{\mathbf{p}}_2$ are given by

$$\hat{\mathbf{p}}_1 = \begin{cases} \tilde{\mathbf{p}}_2, & \mathbf{p}_1^y < \tilde{\mathbf{p}}_2^y \\ \mathbf{p}_1, & \tilde{\mathbf{p}}_2^y \leq \mathbf{p}_1^y \leq \tilde{\mathbf{p}}_1^y, \\ \tilde{\mathbf{p}}_1, & \mathbf{p}_1^y > \tilde{\mathbf{p}}_1^y \end{cases}, \quad \hat{\mathbf{p}}_2 = \begin{cases} \tilde{\mathbf{p}}_2, & \mathbf{p}_2^y < \tilde{\mathbf{p}}_2^y \\ \mathbf{p}_2, & \tilde{\mathbf{p}}_2^y \leq \mathbf{p}_2^y \leq \tilde{\mathbf{p}}_1^y \\ \tilde{\mathbf{p}}_1, & \mathbf{p}_2^y > \tilde{\mathbf{p}}_1^y \end{cases} \quad \text{with} \quad (15)$$

$$\tilde{\mathbf{p}}_1 = \begin{bmatrix} s_1 & -1 \\ \tan \tilde{\theta} & 1 \end{bmatrix}^{-1} \begin{bmatrix} s_1 y_{vs_n} - z_{vs_n} \\ \tan \tilde{\theta} y_l + z_l \end{bmatrix}, \quad \tilde{\mathbf{p}}_2 = \begin{bmatrix} s_2 & -1 \\ \tan \tilde{\theta} & 1 \end{bmatrix}^{-1} \begin{bmatrix} s_2 y_{vs_n} - z_{vs_n} \\ \tan \tilde{\theta} y_l + z_l \end{bmatrix},$$

where \mathbf{a}^y denotes the y component of point \mathbf{a} and $\tilde{\theta} = \theta_r - \theta_{rl}$ is the angle between the lens and the x axis.

Proof: Please refer to Appendix B. ■

²If there is only one IRS, in order to collect maximum power, it is optimal to adjust the lens such that the reflected beam is orthogonal to the lens. However, if there are more than one IRS, the reflected beams from all IRSs cannot be perpendicular to the lens at the Rx at the same time. Therefore, the Rx needs to employ either a large PD (which would lead to a large field of view at the Rx and in turn a higher background noise level [31]) or more than one PD to collect the powers from the directions of the beams arriving from different IRSs. Therefore, to keep our model general, we assume a non-orthogonal reflected beam which includes the orthogonal beam as a special case.

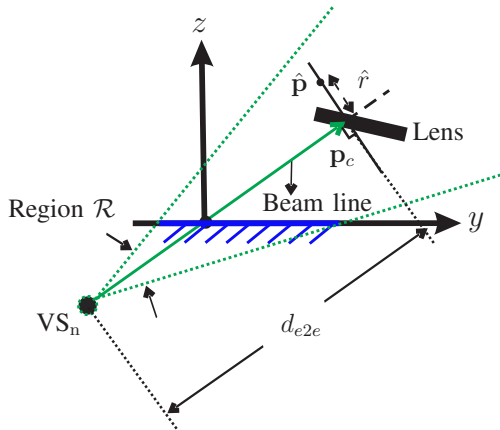


Fig. 4. Schematic representation of Lemma 2.

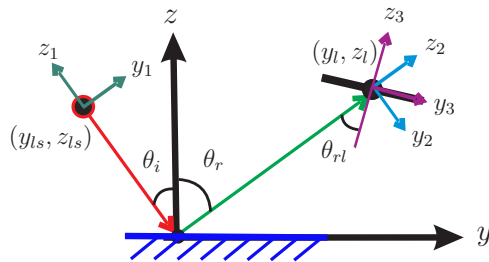


Fig. 5. 2D coordinate systems for characterization of the LS, IRS, and lens fluctuations as well as the misalignment across the lens line.

Note that the conditions under which (14) in Proposition 1 holds are met in practice since 1) the physical size of the lens is much smaller than the transmission distance, i.e., $2a_l \ll d_{e2e}$ holds, and 2) r_c corresponds to the beam misalignment and for a properly designed system, the misalignment is much smaller than the end-to-end transmission distance, i.e., $r_c \ll d_{e2e}$ holds. The impact of the size of the IRS is reflected in the values of ρ_1 and ρ_2 . In fact, if the IRS is sufficiently large such that the lens is located in region \mathcal{R} defined before Lemma 2, we obtain $\rho_1 = \|\mathbf{p}_0 - \mathbf{p}_1\|$, $\rho_2 = \|\mathbf{p}_0 - \mathbf{p}_2\|$.

Corollary 2: For the special case where $\hat{\mathbf{p}}_i = \mathbf{p}_i, i = 1, 2$, i.e., the IRS is sufficiently large, and the reflected beam strikes the center of the lens and its direction is perpendicular to the lens, the conditional GML is given by

$$h_g = \operatorname{erf}\left(\frac{\sqrt{2}a_l}{w(d_{e2e}, \hat{w}_0)}\right). \quad (16)$$

Proof: Eq. (16) is obtained by substituting $\theta_{rl} = 0$ and $\rho_1 = \rho_2 = \|\mathbf{p}_0 - \mathbf{p}_1\| = \|\mathbf{p}_0 - \mathbf{p}_2\| = a_l$ into (14). This completes the proof. ■

For a given lens length a_l , the maximum fraction of power collected by the PD is given by (16). To attain this maximum, three conditions have to hold, namely the IRS is sufficiently large, the misalignment is zero, i.e., $\theta_r = \theta_r^*$, cf. (13), and the lens is orthogonal to the beam line, i.e., $\theta_{rl} = 0$.

IV. STATISTICAL MODEL - 2D SYSTEM

In this section, we study the effect that building sway has on the quality of the considered FSO channel. To this end, we first introduce the considered misalignment model and then derive the probability density function (PDF) of the corresponding GML.

A. Misalignment Model

We assume that the positions of LS, IRS, and lens fluctuate because of building sway in both the y and z directions. In the following, we show that for the LS, IRS, and lens only the fluctuations in a certain direction have a considerable impact on the FSO channel quality, respectively. This observation substantially simplifies the derivation of the proposed statistical GML model. To this end, we define suitable coordinate systems to formally characterize the fluctuations of LS, IRS, and lens, cf. Fig. 5.

LS: The fluctuations of the position of the LS can be projected in two directions, one parallel to the beam line, z_1 , and one orthogonal to it, y_1 , cf. Fig. 5. Let ϵ_s^z and ϵ_s^y denote the fluctuations of the LS position for the former and latter cases, respectively. Hereby, since the fluctuations of the LS in the beam direction are much smaller than the distance between the LS and the IRS, the impact of ϵ_s^z on h_g can be safely neglected.

IRS: The fluctuations of the position of the IRS can also be projected in two directions, one parallel to the IRS line, y , and one orthogonal to it, z . Let ϵ_r^y and ϵ_r^z denote the fluctuations along the y and z axes, respectively. Assuming that the beam line is aligned to pass through the IRS (not necessarily its center) and that the size of the IRS is large, the impact of ϵ_r^y on h_g is negligible.

Lens: Similar to the LS, let ϵ_l^z and ϵ_l^y denote the fluctuations of the position of the lens in the direction of the reflected beam, z_2 , and perpendicular to it, y_2 , respectively. Since the distance between the IRS and the lens is much larger than the fluctuations in the direction of the reflected beam, we can safely neglect the impact of ϵ_l^z on h_g .

The following lemma provides the misalignment between the center of the beam footprint and the center of the lens, denoted by u , in terms of $(\epsilon_s^y, \epsilon_r^z, \epsilon_l^y)$. By convention, we specify u in the direction of the axis y_3 in Fig. 5.

Lemma 3: Misalignment u as a function of $(\epsilon_s^y, \epsilon_r^z, \epsilon_l^y)$ is obtained as

$$u = \frac{1}{\cos \theta_{rl}} \left(\frac{\cos \theta_r}{\cos \theta_i} \epsilon_s^y - \frac{\sin(\theta_i + \theta_r)}{\cos \theta_i} \epsilon_r^z - \epsilon_l^y \right). \quad (17)$$

Proof: The proof follows from deriving the contributions of ϵ_s^y , ϵ_r^z , ϵ_l^y along the y_3 axis. For this, we exploit the fact that a misalignment \hat{a} in the line perpendicular to the beam causes misalignment $\tilde{a} = \frac{\hat{a}}{\sin \theta}$ on a line having angle $\theta \in [0, \frac{\pi}{2}]$ with the beam line. Using this result, lens movement ϵ_l^y along the y_3 axis causes misalignment $\frac{-\epsilon_l^y}{\sin(\frac{\pi}{2} - \theta_{rl})} = \frac{-\epsilon_l^y}{\cos \theta_{rl}}$. For the LS, movement ϵ_s^y causes misalignment $\frac{\epsilon_s^y}{\cos \theta_i}$ along the y axis on the IRS. Further projecting $\frac{\epsilon_s^y}{\cos \theta_i}$ along the y_2 axis yields misalignment $\frac{\epsilon_s^y \cos \theta_r}{\cos \theta_i}$, which in turn causes the overall misalignment $\frac{\epsilon_s^y \cos \theta_r}{\cos \theta_{rl} \cos \theta_i}$ along the y_3 axis on the lens. Furthermore, moving the IRS by ϵ_r^z along the z axis is equivalent to keeping the IRS fixed but having a misalignment of

$-\epsilon_r^z(\tan \theta_i + \tan \theta_r)$ along the y axis on the IRS. Projecting this misalignment first along the y_2 axis and then along the y_3 axis leads to $\frac{-\epsilon_r^z(\tan \theta_i + \tan \theta_r) \cos \theta_r}{\cos \theta_{rl}} = \frac{\epsilon_r^z \sin(\theta_i + \theta_r)}{\cos \theta_{rl} \cos \theta_i}$. This completes the proof. ■

Fluctuations $(\epsilon_s^y, \epsilon_r^z, \epsilon_l^y)$ are typically modelled as RVs. A widely-accepted model for building sway assumes independent zero-mean Gaussian fluctuations [3], [32], i.e., $\epsilon_i^j \sim \mathcal{N}(0, \sigma_i^2)$, $i \in \{s, r, l\}$, $j \in \{y, z\}$, where σ_i^2 denotes the variance of ϵ_i^j . Therefore, from (17), the misalignment also follows a zero-mean Gaussian distribution, i.e., $u \sim \mathcal{N}(0, \sigma_u^2)$ with variance

$$\sigma_u^2 = \frac{1}{\cos^2 \theta_{rl}} \left(\frac{\cos^2 \theta_r}{\cos^2 \theta_i} \sigma_s^2 + \frac{\sin^2(\theta_i + \theta_r)}{\cos^2 \theta_i} \sigma_r^2 + \sigma_l^2 \right). \quad (18)$$

B. PDF of GML

In order to obtain a statistical channel model for the GML h_g , first the power collected by the PD (i.e., the conditional GML) has to be derived as a function of u . To do so, we can use the exact expressions in (14) and replace (ρ_1, ρ_2) with $(|u - a_l|, u + a_l)$, assuming that the IRS is sufficiently large such that the lens is located in region \mathcal{R} defined before Lemma 2. However, the resulting expressions are rather complicated and do not provide useful insights. Thus, to provide insights, we approximate h_g as a function of u as follows

$$h_g \approx A_0 \exp \left(\frac{-2u^2}{tw^2(d_{e2e}, \hat{w}_0)} \right), \quad (19)$$

where $A_0 = \text{erf}(\nu)$, $t = \frac{\sqrt{\pi} \text{erf}(\nu)}{2\nu \exp(-\nu^2) \cos^2 \theta_{rl}}$, and $\nu = \frac{\sqrt{2} \cos \theta_{rl} a_l}{w(d_{e2e}, \hat{w}_0)}$. The derivation of (19) is provided in Appendix C. We verify the accuracy of (19) in Fig. 7 in Section VII. Using this approximation, the PDF of h_g is given in the following proposition.

Proposition 2: Assuming Gaussian fluctuations for the building sway, the PDF of h_g is given by

$$f_{h_g}(h_g) = \frac{\sqrt{\varpi}}{2A_0\sqrt{\pi}} \left[\ln \left(\frac{A_0}{h_g} \right) \right]^{-\frac{1}{2}} \left(\frac{h_g}{A_0} \right)^{\varpi-1}, \quad 0 \leq h_g \leq A_0, \quad (20)$$

where $\varpi = \frac{tw^2(d_{e2e}, \hat{w}_0)}{4\sigma_u^2}$.

Proof: Eq. (20) can be obtained by exploiting the relation between u and h_g in (19) and the fact that u follows a zero-mean Gaussian distribution. ■

V. EXTENSION TO 3D SYSTEM MODEL

Before studying the 3D system, let us first recall the following insights from the analysis of the 2D system, cf. Sections III and IV. *i)* The concept of an equivalent mirror-assisted system enabled us to analyze the original IRS-assisted system using the imaging technique from geometric optics. *ii)* The

effect of beam truncation can be neglected if the IRS is sufficiently large. *iii*) The statistical analysis can be significantly simplified by considering only the components of the Tx, IRS, and Rx fluctuation variables that have a non-negligible impact on the GML. Exploiting these insights, we now extend the models developed so far to the 3D case.

A. Conditional GML

In the following, we first find the power distribution across the IRS. Subsequently, similar to the 2D case, we develop an equivalent mirror-assisted system for the considered 3D system based on which we derive the fraction of power collected by the PD at the Rx (i.e., the conditional GML). To simplify the analysis, we assume that the IRS size is sufficiently large to neglect beam truncation.

1) *Power Distribution*: The following lemma presents the power distribution across the IRS.

Lemma 4: The power distribution of the Gaussian beam originating from the LS at point $\mathbf{a} = (x, y)^\top$ on the IRS is obtained as

$$I_G^{\text{irs}}(x, y | d_{sr}, \Psi_i, w_0) = \frac{2 \cos \theta_i}{\pi w^2(d_{sr}, w_0)} \exp(-2\mathbf{a}^\top \mathbf{S}_{w_0}^{d_{sr}} \mathbf{T}_{\theta_i}^2 \mathbf{a}), \quad (21)$$

where $\mathbf{S}_{w_0}^{d_{sr}} = \frac{1}{w^2(d_{sr}, w_0)} \mathbf{I}_2$.

Proof: Please refer to Appendix D. ■

Note that the contours of the laser beam power distribution across the IRS are ellipsoids whose major and minor axes are the main diagonal elements of $(2\mathbf{S}_{w_0}^{d_{sr}} \mathbf{T}_{\theta_i}^2)^{-1/2}$.

2) *Equivalent Mirror-assisted System*: Similar to the 2D case, the equivalent mirror-assisted system is constructed as follows: *i*) The IRS is replaced by a mirror. *ii*) The LS is replaced by a new LS, denoted by LS_n , which is located in a different position such that it has distance d_{sr} from the mirror and its beam hits the mirror with an incident angle equal to the reflection angle in the original IRS-assisted system, i.e., $\Psi_r = (\theta_r, \phi_r)$. Therefore, from geometric optics, the angle of reflection at the mirror is Ψ_r . *iii*) Unlike the 2D case, in the 3D system, a simple Gaussian beam originating from the LS_n cannot provide the same power distribution across the mirror as that given in (21) for any desired reflection angle $\Psi_r = (\theta_r, \phi_r)$. However, a *rotated astigmatic* Gaussian beam can generate the power distribution in (21) for any Ψ_r . Assuming the same $\hat{x}\hat{y}\hat{z}$ -coordinate system as in Section II.B, an *un-rotated* astigmatic Gaussian beam (also referred to as *orthogonal* or *simple* astigmatic Gaussian beam) propagating in $+\hat{z}$ direction has the following electric field [28]

$$E(\hat{x}, \hat{y}, \hat{z}) = E_0 \exp\left(-\left(\frac{\hat{x}^2}{w^2(\hat{z}, w_{01})} + \frac{\hat{y}^2}{w^2(\hat{z}, w_{02})}\right)\right) \exp(j\phi_{\text{AG}}(\hat{\mathbf{a}}, \hat{z}, \mathbf{w}_0)), \quad \text{with phase} \quad (22)$$

$$\phi_{AG}(\hat{\mathbf{a}}, \hat{z}, \mathbf{w}_0) = -k\hat{z} - k\left(\frac{\hat{x}^2}{2R(\hat{z}, w_{01})} + \frac{\hat{y}^2}{2R(\hat{z}, w_{02})}\right) + \psi(\hat{z}, w_{01}, w_{02}), \quad (23)$$

where w_{01} and w_{02} are the waist radii of the beam and $\mathbf{w}_0 = (w_{01}, w_{02})$. Moreover, $w(\cdot, \cdot)$ and $R(\cdot, \cdot)$ are given in Section II.B, $\hat{\mathbf{a}} = (\hat{x}, \hat{y})^\top$, $\psi(\hat{z}, w_{01}, w_{02}) = \frac{1}{2}\left(\tan^{-1}\left(\frac{\hat{z}}{z_{R1}}\right) + \tan^{-1}\left(\frac{\hat{z}}{z_{R2}}\right)\right)$, and $z_{Ri} = \frac{\pi w_{0i}^2}{\lambda}$. A *rotated astigmatic Gaussian beam* (also referred to as *general astigmatic Gaussian beam*) is obtained from (22) and (23) by substituting $\hat{\mathbf{a}}$ by $\mathbf{R}_\varphi \hat{\mathbf{a}}$, where φ is the angle by which the beam footprint is rotated counter-clockwise. Therefore, the power density of a general astigmatic Gaussian beam across a plane perpendicular to the beam direction, i.e., $+\hat{z}$, is given by

$$I_{AG}^{\text{orth}}(\hat{x}, \hat{y}|\hat{z}, \mathbf{w}_0, \varphi) = I_{AG}^{\text{max}}(\hat{z}, \mathbf{w}_0) \exp\left(-2\hat{\mathbf{a}}^\top \mathbf{R}_\varphi^\top \mathbf{S}_{\mathbf{w}_0}^{\hat{z}} \mathbf{R}_\varphi \hat{\mathbf{a}}\right), \quad (24)$$

where $I_{AG}^{\text{max}}(\hat{z}, \mathbf{w}_0) = \frac{2}{\pi w(\hat{z}, w_{01})w(\hat{z}, w_{02})}$ and $\mathbf{S}_{\mathbf{w}_0}^{\hat{z}} = \text{diag}\left\{\frac{1}{w^2(\hat{z}, w_{01})}, \frac{1}{w^2(\hat{z}, w_{02})}\right\}$.

Corollary 3: Let us consider a new LS whose location is specified by $\hat{\Psi}_i = (\hat{\theta}_i, \hat{\phi}_i)$ and d_{sr} and which emits a general astigmatic Gaussian beam with waist radius parameter $\hat{\mathbf{w}}_0 = (\hat{w}_{01}, \hat{w}_{02})$ and rotation angle $\hat{\varphi}$. Moreover, let λ_i and $\boldsymbol{\nu}_i$ denote the i -th eigenvalue and the corresponding eigenvector of matrix $\mathbf{T}_{\hat{\theta}_i}^{-\top} \mathbf{R}_{\hat{\phi}_i}^\top \mathbf{S}_{\mathbf{w}_0}^{d_{sr}} \mathbf{T}_{\hat{\theta}_i}^2 \mathbf{R}_{\hat{\phi}_i} \mathbf{T}_{\hat{\theta}_i}^{-1}$, respectively. For *any given* $\hat{\Psi}_i$, the power distribution across the IRS caused by the new LS becomes identical to that created by the original LS, i.e.,

$$I_{AG}^{\text{irs}}(x, y|d_{sr}, \hat{\Psi}_i, \hat{\mathbf{w}}_0, \hat{\varphi}) = I_G^{\text{irs}}(x, y|d_{sr}, \Psi_i, w_0), \quad (25)$$

if $\hat{\mathbf{w}}_0 = (\hat{w}_{01}, \hat{w}_{02})$ and $\hat{\varphi}$ are chosen as the solutions to equations $w(d_{sr}, \hat{w}_{0i}) = \frac{1}{\sqrt{\lambda_i}}$, $i = 1, 2$, and $\mathbf{R}_{\hat{\varphi}} = [\boldsymbol{\nu}_1, \boldsymbol{\nu}_2]^\top$, respectively.

Proof: Please refer to Appendix E. ■

The above corollary states that the power distribution across the IRS generated by the LS is equivalent to the power distribution generated by a new LS with *arbitrary* incident angle but with general astigmatic Gaussian beam with waist radii $\hat{\mathbf{w}}_0$ and rotation angle $\hat{\varphi}$ whose values are given in Corollary 3. Therefore, according to Corollary 3 for $\hat{\Psi}_i = \Psi_r$, the power distribution across the IRS and the mirror in the equivalent system are identical.

3) *Phase-shift Design:* The location of LS_n and the properties of its emitted beam (i.e., $\hat{\mathbf{w}}_0$ and $\hat{\varphi}$) determine the phase distribution of the wave reflected by the mirror. Now, we design the phase-shift profile, $\Delta\phi(x, y|\Psi_r, \Psi_i, w_0)$, across the IRS such that the phases of the reflected beams in both systems are the same. This leads to the same reflected electric fields in both systems. Therefore, the angle of reflection in both systems is also identical and is given by Ψ_r .

Proposed Phase-shift Profile: The phase-shift profile that is needed across the IRS to produce an angle

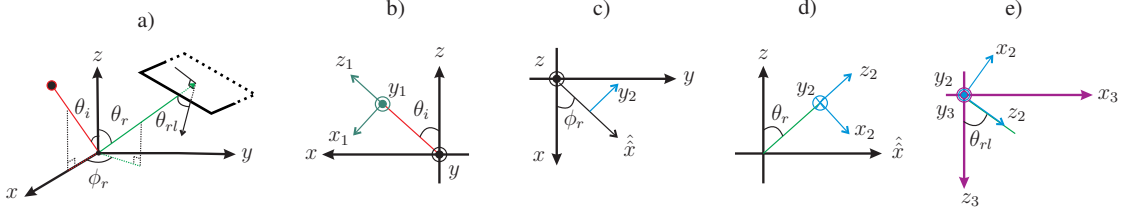


Fig. 6. Illustration of 3D coordinate systems adopted to characterize the LS, IRS, and lens fluctuations as well as the misalignment across the lens plane. a) 3D illustration of the positions of LS, IRS, and lens. b) LS coordinate system, $x_1y_1z_1$, w.r.t. IRS coordinate system, xyz . c) IRS coordinate system, xyz , w.r.t. coordinate system for the plane perpendicular to the reflected beam, $x_2y_2z_2$, in the $x-y$ plane. Here, \hat{x} is the axis perpendicular to the y_2 axis in the IRS plane. d) xyz -coordinate system w.r.t. $x_2y_2z_2$ -coordinate system in the $\hat{x}-z$ plane. e) $x_2y_2z_2$ -coordinate system w.r.t. the lens coordinate system, $x_3y_3z_3$. The same color code is used as in Fig. 5 for the 2D case.

of reflection Ψ_r for an angle of incident Ψ_i is given by

$$\begin{aligned} \Delta\phi(x, y | \Psi_r, \Psi_i, w_0) &= \pi + \phi_{AG}(\mathbf{R}_{\hat{\varphi}} \mathbf{T}_{\theta_r} \mathbf{R}_{-\phi_r} \mathbf{a}, d_{sr} + x \sin \theta_r \cos \phi_r + y \sin \theta_r \sin \phi_r, \hat{\mathbf{w}}_0) \\ &\quad - \phi_G(\sqrt{\mathbf{a}^T \mathbf{T}_{\theta_i} \mathbf{a}}, d_{sr} + x \sin \theta_i, w_0) \stackrel{(a)}{=} \pi + k(x(\sin \theta_i - \sin \theta_r \cos \phi_r) - y \sin \theta_r \sin \phi_r), \end{aligned} \quad (26)$$

where equality (a) holds for the far field, i.e., $d_{sr} \gg \frac{\pi w_0^2}{\lambda}$. Moreover, $\phi_G(\cdot, \cdot, \cdot)$ is the phase of the Gaussian beam originating from the LS, which is given in (2), and $\phi_{AG}(\cdot, \cdot, \cdot)$ is the phase of the general astigmatic Gaussian beam originating from LS_n , which is given in (23). In the following, similar to the 2D case, we use the imaging technique from geometric optics for the equivalent system to obtain the power collected by the PD.

4) *Conditional GML*: Assuming a sufficiently large mirror in the equivalent system, LS_n can be mirrored w.r.t. the mirror plane, creating a virtual LS denoted by VS_n which emits the same beam as LS_n , cf. Corollary 3, and which has distance d_{e2e} from the PD. Then, as shown in Appendix F, the fraction of power collected by the PD (i.e., the conditional GML) is given as follows

$$h_g(u) \approx A_0 \exp\left(-\frac{2\|\mathbf{u}\|^2}{t}\right), \quad (27)$$

where $t = \frac{\pi a_l^2}{4\nu_1\nu_2} \sqrt{\frac{\pi \operatorname{erf}(\nu_1) \operatorname{erf}(\nu_2)}{\nu_1\nu_2 \exp(-(\nu_1^2 + \nu_2^2))}}$, $\nu_1 = a_l \sqrt{\frac{\pi \delta_1}{2}}$, and $\nu_2 = a_l \sqrt{\frac{\pi \delta_2}{2}}$. Here, δ_i , $i = 1, 2$, are the eigenvalues of matrix $\mathbf{T}_{\theta_{rl}}^T \mathbf{R}_{\hat{\varphi}}^T \mathbf{S}_{\hat{\mathbf{w}}_0}^{d_{e2e}} \mathbf{R}_{\hat{\varphi}} \mathbf{T}_{\theta_{rl}}$, where $\mathbf{S}_{\hat{\mathbf{w}}_0}^{d_{e2e}} = \operatorname{diag}\left\{\frac{1}{w^2(d_{e2e}, \hat{w}_{01})}, \frac{1}{w^2(d_{e2e}, \hat{w}_{02})}\right\}$. Moreover, \mathbf{u} denotes the vector of misalignment between the beam footprint center and the center of the lens and A_0 denotes the maximum fraction of optical power captured by the lens at $\|\mathbf{u}\| = 0$ and is given by $A_0 = \frac{\pi^2 \cos \theta_{rl} I_{AG}^{\max}(d_{e2e}, \hat{\mathbf{w}}_0) a_l^2}{4\nu_1\nu_2} \operatorname{erf}(\nu_1) \operatorname{erf}(\nu_2)$. In the following, we derive a statistical GML model based on (27) incorporating the impact of the IRS position fluctuations due to building sway.

B. Statistical GML Model

Similar to the statistical analysis for 2D systems in Section IV, we assume Gaussian fluctuations due to building sway for the LS, IRS, and Rx lens as described in the following. To this end, we define suitable right-handed coordinate systems to formally characterize the fluctuations of LS, IRS, and lens and the overall misalignment across the lens, cf. Fig. 6.

LS: For the LS, fluctuations along the z_1 axis have negligible impact on h_g ; hence, to characterize the fluctuations of the LS position, we need only two variables along the x_1 and y_1 directions, denoted by $\epsilon_s^x, \epsilon_s^y \sim \mathcal{N}(0, \sigma_s^2)$, respectively, cf. Fig. 6b).

IRS: Since we assume a sufficiently large IRS such that beam truncation can be neglected, the fluctuations of the IRS within its plane, i.e., the $x - y$ plane, can be neglected. Therefore, only the fluctuations along the z axis, denoted by $\epsilon_r^z \sim \mathcal{N}(0, \sigma_r^2)$, are considered, cf. Fig. 6c) and d).

Lens: Similar to the LS, the fluctuations along the reflected beam direction, z_2 , can be neglected. Let $\epsilon_l^x, \epsilon_l^y \sim \mathcal{N}(0, \sigma_l^2)$ denote the fluctuations along the x_2 and y_2 axes, respectively, cf. Fig. 6e).

The misalignment vector \mathbf{u} defined in the lens plane, i.e., in the $x_3 - y_3$ plane, is provided in the following lemma.

Lemma 5: The misalignment vector \mathbf{u} as a function of $\epsilon_s^{xy} = (\epsilon_s^x, \epsilon_s^y)^\top$, ϵ_r^z , and $\epsilon_l^{xy} = (\epsilon_l^x, \epsilon_l^y)^\top$ is obtained as follows

$$\mathbf{u} = (u_1, u_2)^\top = \mathbf{T}_{\theta_{rl}}^{-1}(\mathbf{T}_{\theta_r} \mathbf{R}_{-\phi_r} \mathbf{T}_{\theta_i}^{-1} \epsilon_s^{xy} - \mathbf{T}_{\theta_r} \mathbf{R}_{-\phi_r} \mathbf{v} \epsilon_r^z - \epsilon_l^{xy}), \quad (28)$$

where $\mathbf{v} = (\tan \theta_r \cos \phi_r - \tan \theta_i, \tan \theta_r \sin \phi_r)^\top$.

Proof: The proof follows from projecting the LS, IRS, and lens position fluctuations along the lens plane, i.e., in the x_3 and y_3 directions. To this end, we use the following result. Let us consider two coordinate systems $\hat{x}\hat{y}\hat{z}$ and $\tilde{x}\tilde{y}\tilde{z}$, where the latter system is transformed to the former by first counter-clockwise rotation of \tilde{x} and \tilde{y} around the \tilde{z} axis by angle ϕ and then counter-clockwise rotation of the resulting new \tilde{x} axis as well as the \tilde{z} axis around the new \tilde{y} by angle θ . Therefore, θ is the angle between the \hat{z} and \tilde{z} axes and between the \hat{x} and \tilde{x} axes and ϕ is the angle between the \hat{y} and \tilde{y} axes. Let us assume that a beam propagates parallel to the \hat{z} axis and let $\hat{\mathbf{a}}$ denote the misalignment in the $\hat{x} - \hat{y}$ plane. Projecting $\hat{\mathbf{a}}$ into non-perpendicular plane $\tilde{x} - \tilde{y}$ yields misalignment $\tilde{\mathbf{a}}$ which is related to $\hat{\mathbf{a}}$ as $\hat{\mathbf{a}} = \mathbf{T}_\theta \mathbf{R}_{-\phi} \tilde{\mathbf{a}}$. For the lens, projecting fluctuation ϵ_l^{xy} into the $x_3 - y_3$ plane yields misalignment $-(\mathbf{T}_{\theta_{rl}} \mathbf{R}_{-\phi_{rl}})^{-1} \epsilon_l^{xy} = -\mathbf{T}_{\theta_{rl}}^{-1} \epsilon_l^{xy}$, where by definition $\phi_{rl} = 0$. For the LS, fluctuation ϵ_s^{xy} is first transformed into the $x - y$ plane, then into the $x_2 - y_2$ plane, and finally into the $x_3 - y_3$ plane. This leads to misalignment $(\mathbf{T}_{\theta_{rl}} \mathbf{R}_{-\phi_{rl}})^{-1} \mathbf{T}_{2\pi-\theta_r} \mathbf{R}_{-\phi_r} (\mathbf{T}_{\theta_i} \mathbf{R}_{-\phi_i})^{-1} \epsilon_s^{xy} = \mathbf{T}_{\theta_{rl}}^{-1} \mathbf{T}_{\theta_r} \mathbf{R}_{-\phi_r} \mathbf{T}_{\theta_i}^{-1} \epsilon_s^{xy}$,

where we use definitions $\phi_i = \phi_{rl} = 0$. Furthermore, moving the IRS with ϵ_r^z along the z axis is equivalent to keeping the IRS fixed but having a misalignment of $\mathbf{v}\epsilon_r^z$ along the $x - y$ plane on the IRS. Projecting this misalignment first into the $x_2 - y_2$ plane, and then into the $x_3 - y_3$ plane leads to $(\mathbf{T}_{\theta_{rl}}\mathbf{R}_{-\phi_{rl}})^{-1}\mathbf{T}_{2\pi-\theta_r}\mathbf{R}_{-\phi_r}\mathbf{v}\epsilon_r^z = \mathbf{T}_{\theta_{rl}}^{-1}\mathbf{T}_{\theta_r}\mathbf{R}_{-\phi_r}\mathbf{v}\epsilon_r^z$. This completes the proof. \blacksquare

From (28), we observe that \mathbf{u} is a zero-mean bivariate Gaussian RV with covariance matrix

$$\Sigma = \mathbf{T}_{\theta_{rl}}^{-1}(\mathbf{T}_{\theta_r}\mathbf{R}_{-\phi_r}\mathbf{T}_{\theta_i}^{-1}\mathbf{T}_{\theta_i}^{-\top}\mathbf{R}_{-\phi_r}^{\top}\mathbf{T}_{\theta_r}^{\top}\sigma_s^2 + \mathbf{T}_{\theta_r}\mathbf{R}_{-\phi_r}\mathbf{v}\mathbf{v}^{\top}\mathbf{R}_{-\phi_r}^{\top}\mathbf{T}_{\theta_r}^{\top}\sigma_r^2 + \sigma_l^2\mathbf{I}_2)\mathbf{T}_{\theta_{rl}}^{-\top}. \quad (29)$$

Therefore, $\|\mathbf{u}\|$ follows a Hoyt (Nakagami- q) distribution with mean $\Omega = \chi_1 + \chi_2$ and Nakagami- q fading parameter $q = \left[\frac{\min\{\chi_1, \chi_2\}}{\max\{\chi_1, \chi_2\}}\right]^{1/2}$ [32], [33], where χ_1 and χ_2 are the eigenvalues of Σ . Exploiting (27) and (28), the PDF of h_g can be obtained as follows

$$f_{h_g}(h_g) = \frac{\varpi}{A_0} \left(\frac{h_g}{A_0}\right)^{\frac{(1+q^2)\varpi}{2q}-1} I_0\left(-\frac{(1-q^2)\varpi}{2q} \ln\left(\frac{h_g}{A_0}\right)\right), \quad 0 \leq h_g \leq A_0, \quad (30)$$

where $\varpi = \frac{(1+q^2)t}{4q\Omega}$ is a constant.

Corollary 4: For the special case where $\phi_r = \pi$ and $\theta_{rl} = 0$, the misalignment \mathbf{u} simplifies to

$$\mathbf{u} = \left(\frac{\cos\theta_r}{\cos\theta_i}\epsilon_s^x - \frac{\sin(\theta_i + \theta_r)}{\cos\theta_i}\epsilon_r^z - \epsilon_l^x, \epsilon_s^y - \epsilon_l^y\right), \quad (31)$$

which is again a zero-mean bivariate Gaussian RV. Therefore, the GML follows the distribution given in (30) with parameters $q = \left[\frac{\min\{\sigma_{u_1}^2, \sigma_{u_2}^2\}}{\max\{\sigma_{u_1}^2, \sigma_{u_2}^2\}}\right]^{1/2}$ and $\Omega = \sigma_{u_1}^2 + \sigma_{u_2}^2$, where $\sigma_{u_1}^2 = \frac{\cos^2\theta_r}{\cos^2\theta_i}\sigma_s^2 + \frac{\sin^2(\theta_i + \theta_r)}{\cos^2\theta_i}\sigma_r^2 + \sigma_l^2$ and $\sigma_{u_2}^2 = \sigma_s^2 + \sigma_l^2$. In this case, the parameters in (27) simplify as follows. In particular, $A_0 = \text{erf}(\nu_1)\text{erf}(\nu_2)$ and $\delta_i = \frac{1}{w^2(d_{sr}, \hat{w}_{0_i})}$ hold, where \hat{w}_{0_i} , $i = 1, 2$, are given as the solution of $w(d_{sr}, \hat{w}_{0_1}) = \left|\frac{\cos\theta_r}{\cos\theta_i}\right|w(d_{sr}, w_0)$ and $w(d_{sr}, \hat{w}_{0_2}) = w(d_{sr}, w_0)$, respectively. When only the IRS moves, i.e., $\sigma_s = 0$ and $\sigma_l = 0$ hold, the misalignment becomes a scalar. In this case, the magnitude of the misalignment is given by $|u| = \left|\frac{\sin(\theta_i + \theta_r)}{\cos\theta_i}\epsilon_r^z\right|$ which follows a single-sided Gaussian distribution, i.e., $f_{|u|}(x) = \frac{\sqrt{2}}{\sqrt{\pi\sigma_t^2}} \exp\left(-\frac{x^2}{2\sigma_t^2}\right)$, where $\sigma_t^2 = \frac{\sin^2(\theta_i + \theta_r)}{\cos^2\theta_i}\sigma_r^2$. Therefore, h_g follows the following distribution

$$f_{h_g}(h_g) = \frac{\sqrt{\varrho}}{\sqrt{\pi}A_0} \left(\frac{h_g}{A_0}\right)^{\varrho-1} \left[\ln\left(\frac{A_0}{h_g}\right)\right]^{-1/2}, \quad 0 \leq h_g \leq A_0, \quad (32)$$

where $\varrho = \frac{t}{4\sigma_t^2}$.

Remark 2: In the case of a simple mirror instead of an IRS, $\phi_r = \pi$ and $\theta_r = \theta_i$ hold. Therefore, in order to provide a desired angle of reflection, unlike the IRSs, the mirror has to mechanically rotate [1]. In this case, the PDF of the GML is the same as in (30) with $q = \left[\frac{\sigma_s^2 + \sigma_l^2}{\sigma_s^2 + \sigma_l^2 + 4\sigma_r^2 \sin^2\theta_i}\right]^{1/2}$ and $\Omega = 2\sigma_s^2 + 2\sigma_l^2 + 4\sigma_r^2 \sin^2\theta_i$ [1].

VI. OUTAGE PROBABILITY OF THE 3D MODEL

Due to the high data rates of FSO systems, the channel coherence time, which is in the order of a few milliseconds, is much longer than a symbol interval. Therefore, the outage probability is a relevant metric to evaluate the performance of FSO systems in the presence of atmospheric turbulence and GML [31]. The outage probability is defined as the probability that the SNR, given by $\gamma = h^2\bar{\gamma}$ with transmit SNR $\bar{\gamma} = \frac{P^2}{\sigma_n^2}$, falls below a predefined threshold, γ_{thr} , whose value depends on the adopted transmission scheme and the application of interest. The outage probability can be computed as follows

$$P_{\text{out}} = \Pr\{\gamma \leq \gamma_{\text{thr}}\} = \Pr\{h^2\bar{\gamma} \leq \gamma_{\text{thr}}\} = \int_0^{\sqrt{\gamma_{\text{thr}}/\bar{\gamma}}} f_h(h)dh, \quad (33)$$

where $f_h(h)$ denotes the PDF of the composite channel given in (6). This PDF can be expressed in terms of the following finite integral

$$f_h(h) = \int_0^1 \frac{1}{\eta h_p x} f_{h_g}(A_0 x) f_{h_a}\left(\frac{h}{\eta h_p A_0 x}\right) dx, \quad (34)$$

where $f_{h_g}(h_g)$ is given in (30) and $f_{h_a}(h_a)$ denotes the PDF of the atmospheric turbulence which is given by

$$f_{h_a}(h_a) = \begin{cases} \frac{1}{\sqrt{8\pi\sigma^2 h_a}} \exp\left(-\frac{(\ln(h_a)+2\sigma^2)^2}{8\sigma^2}\right), & \text{LN} \\ \frac{2(\alpha\beta h_a)^{\frac{\alpha+\beta}{2}}}{\Gamma(\alpha)\Gamma(\beta)h_a} K_{\alpha-\beta}\left(2\sqrt{\alpha\beta h_a}\right), & \text{GG.} \end{cases} \quad (35)$$

In (35), σ^2 is given by $\sigma^2 \approx \frac{\sigma_R^2}{4}$, where $\sigma_R^2 = 1.23C_n^2 k^{7/6} d_{e2e}^{11/6}$ is the Rytov variance, C_n^2 is the index of refraction structure parameter, and α and β are given as follows [2]

$$\alpha = \left[\exp\left(\frac{0.49\sigma_R^2}{(1+1.11\sigma_R^{12/5})^{7/6}}\right) - 1 \right]^{-1} \quad \text{and} \quad \beta = \left[\exp\left(\frac{0.51\sigma_R^2}{(1+0.69\sigma_R^{12/5})^{5/6}}\right) - 1 \right]^{-1}. \quad (36)$$

Note that turbulence conditions can be categorized into two regimes according to the Rytov variance, namely, weak turbulence ($\sigma_R^2 < 0.3$) which is modelled by the LN distribution and moderate-to-strong turbulence ($\sigma_R^2 \geq 0.3$) which is modelled by the GG distribution [33]. Unfortunately, the composite fading PDF in (34) cannot be computed in closed form. However, it involves only one finite integral that can be easily computed numerically. The outage probability for LN and GG turbulence induced fading is given in the following for 3D systems.

1) *LN Fading*: The outage probability of an IRS-assisted FSO link assuming LN distributed atmospheric turbulence induced fading is obtained by substituting $f_{h_a}(\cdot)$ for LN fading in (35) into (33) and

TABLE I
SIMULATION PARAMETERS [9], [31].

Symbol	λ	κ	η	ζ	d_{e2e}	(θ_i, ϕ_i)	(θ_r, ϕ_r)	θ_{rl}	a_l	a_r	(y_{ls}, z_{ls})	(y_r, z_r)	(y_l, z_l)
Value	1550 nm	$0.43 \times 10^{-3} \text{ m}^{-1}$	0.5	1	900 m	$(\frac{\pi}{6}, 0)$ rad	$(\frac{\pi}{5}, \frac{\pi}{8})$ rad	$\frac{\pi}{6}$ rad	2.5 cm	10 cm	(-200, 346) m	(0, 0)	(300, 412) m

(34) as follows

$$P_{\text{out}} = \frac{\varpi}{2} \int_0^1 x^{\frac{(1+q^2)\varpi}{2q}-1} I_0\left(-\frac{(1-q^2)\varpi}{2q} \ln(x)\right) \times \left[1 - \text{erf}\left(\frac{0.5 \ln\left(\frac{\bar{\gamma}}{\gamma_{\text{thr}}}\right) + \ln(\eta h_p A_0 x) - 2\sigma^2}{\sqrt{8\sigma^2}}\right)\right] dx. \quad (37)$$

2) *GG Fading*: Similarly, the outage probability of an IRS-assisted FSO link assuming GG distributed atmospheric turbulence induced fading is obtained as follows

$$P_{\text{out}} = \frac{\pi\varpi}{\sin(\pi(\alpha - \beta))} \int_0^1 x^{\frac{(1+q^2)\varpi}{2q}-1} I_0\left(-\frac{(1-q^2)\varpi}{2q} \ln(x)\right) (f(\alpha, \beta, x) - f(\beta, \alpha, x)) dx, \quad (38)$$

with $f(\alpha, \beta, x) = \frac{1}{\Gamma(\alpha)} \left(\frac{\alpha\beta\sqrt{\gamma_{\text{thr}}/\bar{\gamma}}}{\eta h_p A_0}\right)^\beta x^{-\beta} {}_1\tilde{F}_2\left(\beta; \beta - \alpha + 1, \beta + 1; \frac{\alpha\beta\sqrt{\gamma_{\text{thr}}/\bar{\gamma}}}{\eta h_p A_0 x}\right),$

where ${}_p\tilde{F}_q(a_1, \dots, a_l; b_1, \dots, b_q; z)$ denotes the regularized hypergeometric function which is given by ${}_p\tilde{F}_q(a_1, \dots, a_l; b_1, \dots, b_q; z) = \frac{{}_pF_q(a_1, \dots, a_l; b_1, \dots, b_q; z)}{\Gamma(b_1)\dots\Gamma(b_q)}$ [34].

VII. SIMULATION RESULTS

Unless stated otherwise, the default values of the parameters used in our simulations are given in Table 1. The simulation results reported in Figs. 8, 9, and 10 were obtained based on Monte Carlo simulation and 10^7 realizations of RVs $\epsilon_i^j, i \in \{s, r, l\}, j \in \{x, y, z\}$.

First, in Figs. 7a) and 7b), we study the impact of the size of the IRS on the conditional GML in (14) for two normalized beamwidths at the Rx, namely $\frac{w(d_{e2e}, w_0)}{2a_l} \in \{2, 4\}$. In particular, we show h_g vs. the normalized misalignment $u_n = \frac{u}{2a_l}$ for IRS lengths of $a_r = 5, 10$ cm. As expected, in both figures, we observe that by increasing the magnitude of u_n , the channel gain h_g decreases. Moreover, beam truncation occurs if the normalized misalignment exceeds a certain critical value denoted by u_n^{crt} , i.e., when a part of the lens leaves the truncation region \mathcal{R} given before Lemma 2. In Fig. 7, we use dot-dashed and dashed lines to indicate u_n^{crt} for $a_r = 5$ cm and $a_r = 10$ cm, respectively. Fig. 7 shows that the proposed approximation in (19) is accurate when beam truncation does not occur, i.e., for $|u_n| \leq u_n^{\text{crt}}$. However, since the approximation neglects beam truncation, it overestimates h_g when beam truncation does occur, i.e., for $|u_n| > u_n^{\text{crt}}$. Moreover, we observe that, for $a_r = 10$ cm, the impact of beam truncation shows itself at larger values of $|u_n|$ compared to $a_r = 5$ cm, i.e., $u_n^{\text{crt}} = 1.8$ holds for $a_r = 5$ cm and $u_n^{\text{crt}} = 4$

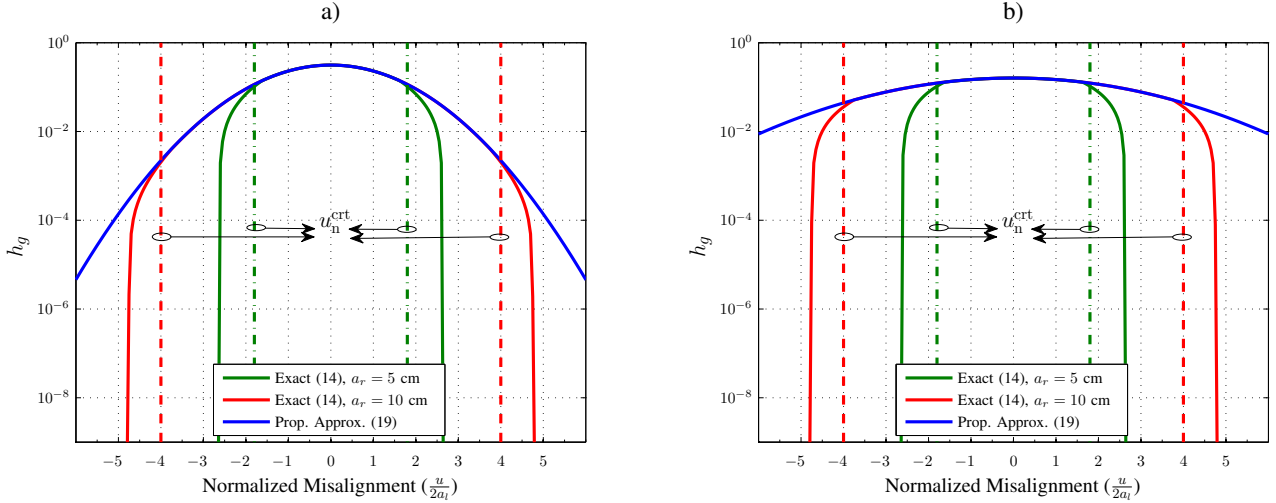


Fig. 7. Conditional GML vs. normalized misalignment $u_n = \frac{u}{2a_l}$ for different IRS sizes a) $\frac{w(d_{e2e}, w_0)}{2a_l} = 2$ and b) $\frac{w(d_{e2e}, w_0)}{2a_l} = 4$.

holds for $a_r = 10$ cm. Furthermore, Fig. 7 shows that for a reasonable size of the IRS, e.g., $a_r > 10$ cm for the considered d_{e2e} (900 m) and a_l (2.5 cm), the proposed approximation is accurate even for large misalignment magnitudes ($|u_n| \leq u_n^{\text{crt}}$, where $u_n^{\text{crt}} > 4$). Finally, comparing Figs. 7a) with $\frac{w(d_{e2e}, w_0)}{2a_l} = 2$ and 7b) with $\frac{w(d_{e2e}, w_0)}{2a_l} = 4$, we observe that the maximum value of h_g in Fig. 7a) is larger than that in Fig. 7b). Moreover, h_g in Fig. 7a) is more sensitive to misalignment and decays dramatically as the magnitude of the misalignment increases. In other words, in case of no misalignment, it is preferable to have a narrower beam to get a larger h_g and in case of severe misalignment, having a wider beam increases the robustness to the misalignment, although a fraction of power is lost due to beam divergence.

Next, in Figs. 8a) and 8b), we study the accuracy of the proposed statistical models for 2D and 3D systems given in (20) and (30), respectively. For the simulation results, we plot the histogram of h_g given by (14) and (27) for 2D and 3D systems, respectively. Fig. 8 shows the PDF of h_g for two normalized beamwidths, namely $\frac{w(d_{e2e}, w_0)}{2a_l} \in \{2, 4\}$, and for four fluctuation scenarios, namely, Scenario 1: $(\sigma_s, \sigma_r, \sigma_l) = 0.5(a_l, a_l, a_l)$ where the building sway for the Tx, IRS, and Rx are equal; Scenario 2: $(\sigma_s, \sigma_r, \sigma_l) = 0.5(3a_l, a_l, a_l)$ where the building sway for the Tx is more severe than that for the IRS and Rx; Scenario 3: $(\sigma_s, \sigma_r, \sigma_l) = 0.5(a_l, 3a_l, a_l)$ where the building sway for the IRS is more severe than that for the Tx and Rx; Scenario 4: $(\sigma_s, \sigma_r, \sigma_l) = 0.5(a_l, a_l, 3a_l)$ where the building sway for the Rx is more severe than that for the Tx and IRS. First, we note that Fig. 8 shows an excellent agreement between the proposed analytical statistical models and the simulation results for both the 2D and 3D systems. This is due to the fact that the impact of beam truncation, which has been neglected in the analysis, is negligible as it occurs with small probability for the considered parameter values. Comparing Scenarios 2-4 with Scenario 1 shows that, for a given beamwidth, increasing the variance

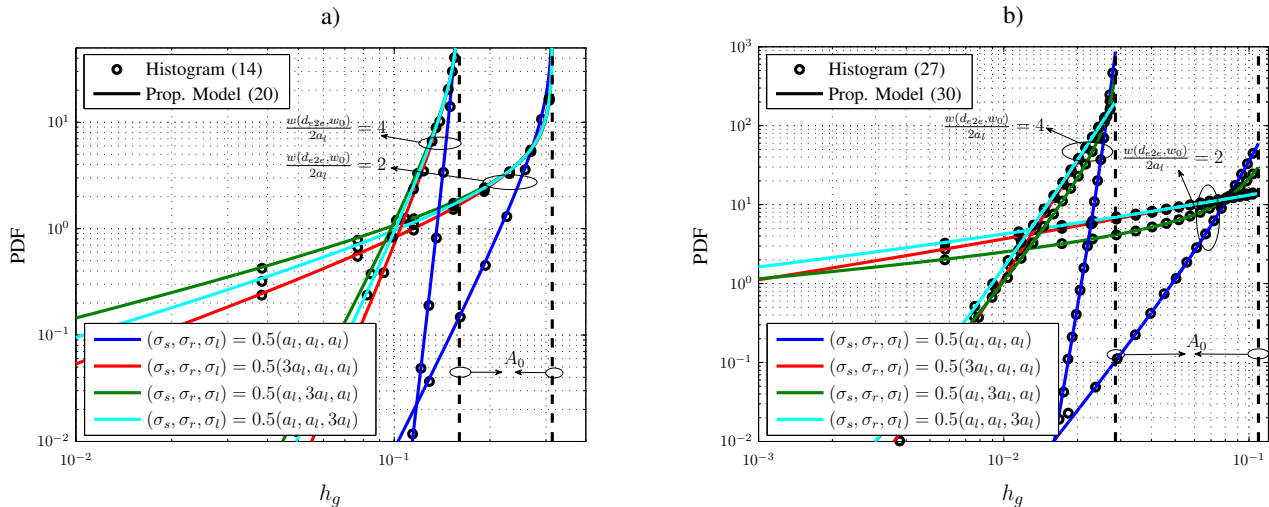


Fig. 8. PDF of the GML for a) 2D and b) 3D system models.

of the fluctuations deteriorates the channel quality, i.e., the probability of having smaller channel gains increases and the PDF becomes more heavily tailed. Moreover, we observe from Fig. 8a) that, for the 2D case and a given beamwidth, the building sway of the IRS has the largest impact and building sway of the Tx has the smallest impact on h_g . On the other hand, for the 3D case and a given beamwidth, the building sway of the Rx has the largest impact and building sway of the IRS has the smallest impact on h_g in Fig. 8b). The different behaviors in the 2D and 3D cases can be understood by investigating the statistics of their corresponding misalignments u and \mathbf{u} , respectively. In particular, for the 2D case, the standard deviation (SD) of u is given by $\sigma_u = 1.08\sigma_s + 1.22\sigma_r + 1.15\sigma_l$, cf. (18), and for the 3D case, the SDs of the components of \mathbf{u} are given by $(\sigma_{u_1}, \sigma_{u_2}) = (1.05, 1.02)\sigma_s + (1.17, 0.2)\sigma_r + (1.15, 1)\sigma_l$, cf. (28). Therefore, for the 2D case, σ_r has the largest impact on the misalignment, whereas for the 3D case, σ_l is more important. Finally, in both figures, for a given scenario, the wider the beam is, the shorter the tail of the PDF becomes, and the smaller the maximum value of h_g , denoted by A_0 (which is denoted by dashed lines in Fig. 8). This is in-line with our observations from Fig. 7.

In Figs. 9 and 10, we plot the outage probability of an IRS-assisted FSO link for the 3D system. In particular, Fig. 9 shows P_{out} vs. the average received SNR for two normalized beamwidths, namely $\frac{w(d_{e2e}, w_0)}{2a_l} \in \{2, 4\}$, and for LN and GG turbulence. From Fig. 9, we observe that the simulation results match the analytical results for both LN and GG atmospheric turbulence. Moreover, the wider beam, i.e., $\frac{w(d_{e2e}, w_0)}{2a_l} = 4$, leads to a smaller P_{out} for high SNRs, since a wider beam is more robust against severe fluctuations.

Finally, we study the impact of the position of the IRS. The simulation setup for Fig. 10b) is depicted in Fig. 10a). In particular, we assume that the Tx, IRS, and Rx are located in the $x - y$ plane at the same altitude. The location of the IRS changes on the upper perimeter of an ellipse with width 1000 m

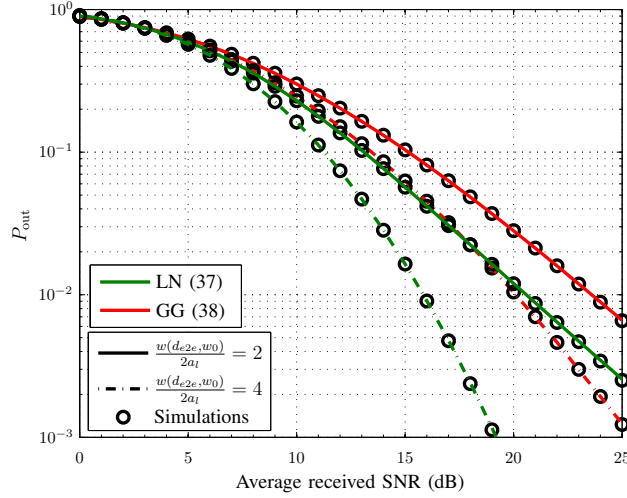


Fig. 9. Outage probability vs. average received SNR for $d_{sr} = 500$ m, $d_{rl} = 600$ m, $\sigma_s = \sigma_r = \sigma_l = 0.75a_l$, and $C_n^2 = 10^{-14} \text{ m}^{\frac{2}{3}}$ and $C_n^2 = 1.4 \times 10^{-14} \text{ m}^{\frac{2}{3}}$ for LN and GG fading, respectively.

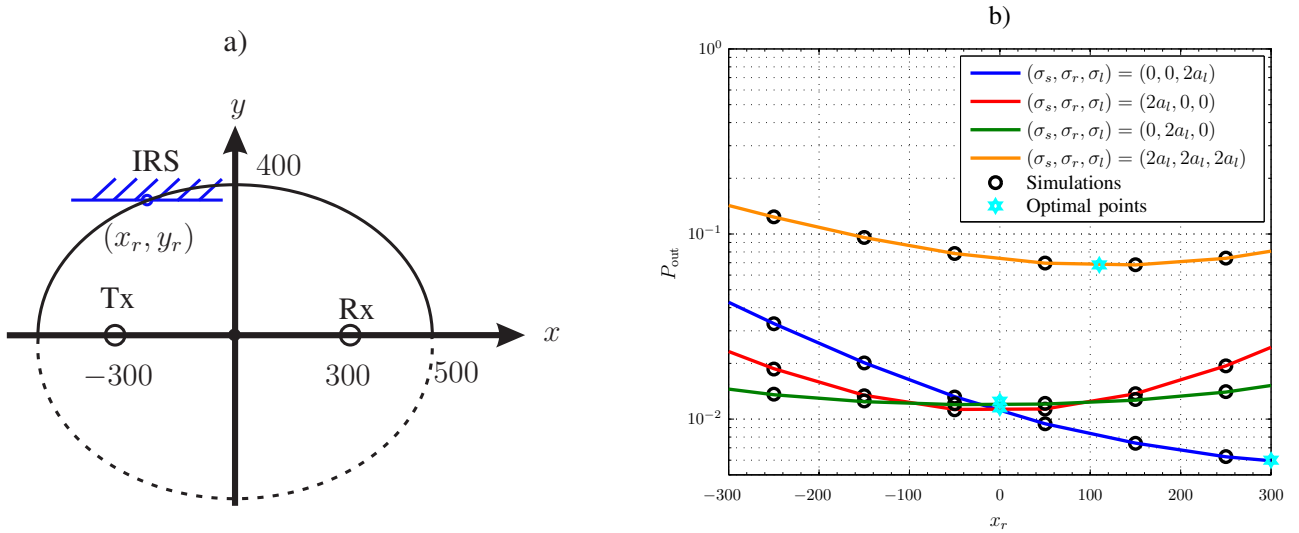


Fig. 10. a) Simulation setup for Fig. 10b) and b) Outage probability vs. x_r for GG atmospheric turbulence ($C_n^2 = 1.7 \times 10^{-14} \text{ m}^{\frac{2}{3}}$, $d_{e2e} = 1000$ m, and $\frac{w(d_{e2e}, w_0)}{2a_l} = 4$).

and height 800 m such that the end-to-end distance that the beam travels between the Tx and Rx, d_{e2e} , is constant, i.e., $d_{e2e} = 1000$ m. Tx and Rx are located at the foci of the ellipse as shown in Fig. 10a). Moreover, we assume that the IRS is always parallel to the $x-z$ plane, the lens plane is always orthogonal to the beam line, i.e., $\theta_{rl} = 0$, and $\phi_r = \pi$ holds. This is in fact the special case studied in Corollary 4. Fig. 10b) shows P_{out} vs. the location of the IRS, x_r , for an average received SNR of 20 dB and for four fluctuation scenarios, namely Scenario 1: $(\sigma_s, \sigma_r, \sigma_l) = (0, 0, 2a_l)$, Scenario 2: $(\sigma_s, \sigma_r, \sigma_l) = (2a_l, 0, 0)$, Scenario 3: $(\sigma_s, \sigma_r, \sigma_l) = (0, 2a_l, 0)$, and Scenario 4: $(\sigma_s, \sigma_r, \sigma_l) = (2a_l, 2a_l, 2a_l)$. We note that by increasing x_r , θ_i and θ_r become larger and smaller, respectively. Therefore, factors $\frac{\cos \theta_r}{\cos \theta_i}$ and $\frac{\sin(\theta_i + \theta_r)}{\cos \theta_i}$

in Corollary 4 increase, which affects the following two system parameters: *i)* The variances of the misalignment caused by the Tx and the IRS building sway increase, cf. (31), which has a negative impact on P_{out} , cf. Fig. 8. Note that since it is assumed that the reflected beam is always orthogonal to the lens at the Rx, the variance of the misalignment caused by the Rx does not change when the IRS is moved. *ii)* The width of the reflected beam becomes wider, cf. $w(d_{sr}, \hat{w}_{0_1})$ in Corollary 4, which has a positive effect on P_{out} for high SNRs, cf. Fig. 9. Therefore, for Scenario 1 where only the second effect exists, P_{out} decreases, as the IRS moves closer to the Rx. However, for Scenarios 2 and 3, due to the competing interplay of both effects, P_{out} first decreases and then increases as x_r increases. Finally, for Scenario 4, the superposition of the misalignment caused by the Tx, IRS, and Rx leads to an optimal position for the IRS at $x_r = 110$ m. By comparing Scenarios 1-3, we also observe that although the building sways of the Tx, IRS, and Rx have identical variances, their relative impacts on P_{out} for a given position of the IRS are not necessarily the same and depend on the relative positioning of the buildings, cf. (31) in Corollary 4. For example, when the IRS is closer to the Tx ($x_r \leq -100$ m), the building sway of the Rx has the largest impact and the building sway of the IRS has the smallest impact on P_{out} .

VIII. CONCLUSIONS

In this paper, we proposed IRS-assisted FSO systems which can overcome the requirement of having a LOS between Tx and Rx. We analyzed 2D and 3D systems by studying equivalent mirror-assisted systems whose reflected electric fields are identical to those of the corresponding IRS-assisted systems employing the phase-shift design proposed in this paper. Based on these analyses, we developed conditional and statistical GML models which characterize the impact of the physical parameters of the IRS, such as its size, position, and orientation, on the end-to-end FSO channel. Moreover, we analyzed the outage probability of an IRS-assisted FSO link assuming that, in addition to the GML, atmospheric turbulence induced fading is also present. Simulation results validated the presented analysis and revealed important insights for system design. For instance, for a reasonable IRS size, e.g. 10 cm for an end-to-end distance in the order of 1 km, the beam truncation caused by the finite-size IRS can be safely neglected. Moreover, we showed via both simulations and theoretical analysis that even if the variances of the fluctuations of the Tx, IRS, and Rx positions are identical, their impact on the end-to-end channel is not necessarily the same and depends on the relative positioning of the three nodes.

APPENDIX A

We use the fact that each point on the IRS is also located on another line, i.e., \tilde{y} , which is orthogonal to the beam line. Moreover, let $I_G^{\text{irs}}(y|d_{sr}, \theta_i, w_0)dy$ denote the fraction of power collected on the infinites-

imally small line element dy around point y on the IRS. Then, due to conservation of energy, we have

$$I_G^{\text{irs}}(y|d_{sr}, \theta_i, w_0)dy = I_G^{\text{orth}}(\tilde{y}|d, w_0)d\tilde{y}, \quad \text{with} \quad d\tilde{y} = \cos \theta_i dy, \quad (39)$$

where $I_G^{\text{orth}}(\tilde{y}|d, w_0)d\tilde{y}$ denotes the fraction of power collected on the infinitesimally small line segment $d\tilde{y}$ around point $(\tilde{y}, 0)$ on a plane orthogonal to the beam line at distance d from the LS. Moreover, from geometry, $d = d_{sr} + y \sin \theta_i$ and $\tilde{y} = y \cos \theta_i$ hold. However, since $d_{sr} \gg y \sin \theta_i$ holds in practice, we approximate $d \approx d_{sr}$. Therefore, (39) simplifies to

$$\begin{aligned} I_G^{\text{irs}}(y|d_{sr}, \theta_i, w_0) &= \cos \theta_i I_G^{\text{orth}}(\cos \theta_i y|d_{sr}, w_0) \\ &= \frac{\sqrt{2} \cos \theta_i}{\sqrt{\pi} w(d_{sr}, w_0)} \exp\left(-\frac{2 \cos^2 \theta_i y^2}{w^2(d_{sr}, w_0)}\right) \stackrel{(a)}{=} I_G^{\text{orth}}(y|d_{sr}, \tilde{w}_0), \end{aligned} \quad (40)$$

where equation (a) follows from comparing $\frac{\sqrt{2} \cos \theta_i}{\sqrt{\pi} w(d_{sr}, w_0)} \exp\left(\frac{-2 \cos^2 \theta_i y^2}{w^2(d_{sr}, w_0)}\right)$ with (4) and \tilde{w}_0 given in (9). This completes the proof.

APPENDIX B

To calculate the fraction of power that flows into the lens (i.e., the conditional GML), we first find the reflected power density across the lens and then integrate it over the lens. Similar to (40) in Appendix A, the reflected power density across the lens is obtained from the reflected power density across the plane perpendicular to the reflected beam, $I_{\text{rf}}^{\text{orth}}(\cdot|\cdot, \cdot)$ given in (12), as $\cos \theta_{rl} I_{\text{rf}}^{\text{orth}}(\rho \cos \theta_{rl}|d_{e2e}, \hat{w}_0)$. By integrating $\cos \theta_{rl} I_{\text{rf}}^{\text{orth}}(\rho \cos \theta_{rl}|d_{e2e}, \hat{w}_0)$ over the lens, the conditional GML is obtained as

$$h_g = \cos \theta_{rl} \begin{cases} \int_0^{\rho_1} I_{\text{rf}}^{\text{orth}}(\rho \cos \theta_{rl}|d_{e2e}, \hat{w}_0)d\rho + \int_0^{\rho_2} I_{\text{rf}}^{\text{orth}}(\rho \cos \theta_{rl}|d_{e2e}, \hat{w}_0)d\rho, & \text{if } \rho_{12} = 2a_l \\ \left| \int_0^{\rho_1} I_{\text{rf}}^{\text{orth}}(\rho \cos \theta_{rl}|d_{e2e}, \hat{w}_0)d\rho - \int_0^{\rho_2} I_{\text{rf}}^{\text{orth}}(\rho \cos \theta_{rl}|d_{e2e}, \hat{w}_0)d\rho \right|, & \text{otherwise,} \end{cases} \quad (41)$$

where ρ_1 , ρ_2 , and ρ_{12} are given in Proposition 1. The two cases in (41) correspond to whether or not the center of the beam footprint lies on the lens line. Substituting $\int_0^{\rho_i} \cos \theta_{rl} I_{\text{rf}}^{\text{orth}}(\rho \cos \theta_{rl}|d_{e2e}, \hat{w}_0)d\rho = \frac{1}{2} \text{erf}\left(\frac{\sqrt{2} \cos \theta_{rl} \rho_i}{w(d_{e2e}, \hat{w}_0)}\right)$ into (41) leads to (14) and concludes the proof.

APPENDIX C

The fraction of power that is collected by the PD as a function of the distance between the lens center and the beam footprint center, denoted by u , is obtained as follows

$$h_g = \int_{-a_l-u}^{a_l-u} \cos \theta_{rl} I_{\text{rf}}^{\text{orth}}(\rho \cos \theta_{rl}|d_{e2e}, \hat{w}_0)d\rho \stackrel{(a)}{=} \int_{-a_l-u}^{a_l-u} \frac{\sqrt{2} \cos \theta_{rl}}{\sqrt{\pi} w(d_{e2e}, \hat{w}_0)} \exp\left(-\frac{2 \cos^2 \theta_{rl} \rho^2}{w^2(d_{e2e}, \hat{w}_0)}\right) d\rho, \quad (42)$$

where $\cos \theta_{rl} I_{\text{rfl}}^{\text{orth}}(\rho \cos \theta_{rl} | d_{e2e}, \hat{w}_0)$ is the reflected power distribution across the lens, see Appendix B, and equality (a) is obtained using (12). In order to approximate h_g , we first use the Taylor series expansion of the exponential term and then simplify it as follows

$$h_g = \frac{\sqrt{2} \cos \theta_{rl}}{\sqrt{\pi} w(d_{e2e}, \hat{w}_0)} \sum_{n=0}^{\infty} \int_{-a_l-u}^{a_l-u} \frac{\left(-\frac{2 \cos^2 \theta_{rl} \rho^2}{w^2(d_{e2e}, \hat{w}_0)}\right)^n}{n!} d\rho = \sum_{n=0}^{\infty} \frac{\frac{\sqrt{2} \cos \theta_{rl}}{\sqrt{\pi} w(d_{e2e}, \hat{w}_0)} \left(-\frac{2 \cos^2 \theta_{rl}}{w^2(d_{e2e}, \hat{w}_0)}\right)^n}{n!(2n+1)} \\ \times \left((a_l - u)^{2n+1} + (a_l + u)^{2n+1} \right) = \sum_{k=0}^{\infty} A_{2k} \left(\frac{\sqrt{2} \cos \theta_{rl} u}{w(d_{e2e}, \hat{w}_0)} \right)^{2k}, \quad (43)$$

where $A_{2k} = \sum_{n=k}^{\infty} \frac{2(-1)^n \binom{2n+1}{2k}}{\sqrt{\pi} n! (2n+1)} \left(\frac{\sqrt{2} \cos \theta_{rl} a_l}{w(d_{e2e}, \hat{w}_0)} \right)^{2n+1-2k}$. By equating the first two terms of (43) to the same terms in the Taylor series expansion of a Gaussian pulse of the form $c \exp\left(\frac{-2u^2}{tw^2(d_{e2e}, \hat{w}_0)}\right)$, where c and t are constants, we obtain (19). This completes the proof.

APPENDIX D

We first present the following lemma which is useful for derivation of the power distribution across the IRS and later for derivation of the power distribution across the lens in Appendix F.

Lemma 6: Consider a $\tilde{x}\tilde{y}\tilde{z}$ -coordinate system. Assume an LS is located at distance \tilde{d} from the origin and its beam line strikes the origin with incident angle $\hat{\Psi}_i = (\hat{\theta}_i, \hat{\phi}_i)$. Let $I^{\text{orth}}(\hat{x}_0, \hat{y}_0 | d)$ denote the power distribution of the general beam (e.g., normal Gaussian and astigmatic Gaussian) at point $\hat{\mathbf{a}} = (\hat{x}_0, \hat{y}_0)^\top$ across a plane perpendicular to the beam line at distance d from the LS. The power distribution at point $\tilde{\mathbf{a}} = (\tilde{x}_0, \tilde{y}_0)^\top$ in the $\tilde{x} - \tilde{y}$ plane is given by

$$I(\tilde{x}_0, \tilde{y}_0 | \tilde{d}, \hat{\Psi}_i) = \cos \hat{\theta}_i I^{\text{orth}}(\hat{x}_0, \hat{y}_0 | \tilde{d}) \quad \text{with} \quad \tilde{\mathbf{a}} = \mathbf{T}_{\hat{\theta}_i} \mathbf{R}_{-\hat{\phi}_i} \hat{\mathbf{a}}. \quad (44)$$

Proof: We use the fact that each point on a plane, which is non-perpendicular to the beam direction, denoted by P_{np} , is also located on another plane, which is perpendicular to the beam line, denoted by P_p . Let $(\tilde{x}_0, \tilde{y}_0)$ and (\hat{x}_0, \hat{y}_0) denote the same point in planes P_{np} and P_p , respectively, expressed in their respective coordinate systems. Moreover, let $I(\tilde{x}_0, \tilde{y}_0 | \tilde{d}, \hat{\Psi}_i) d\tilde{x}d\tilde{y}$ denote the fraction of power collected on the infinitesimally small surface element $d\tilde{x}d\tilde{y}$ around the point $(\tilde{x}_0, \tilde{y}_0)$ on P_{np} with distance \tilde{d} from the LS. Then, due to the conservation of energy, the following relation has to hold

$$I(\tilde{x}_0, \tilde{y}_0 | \tilde{d}, \hat{\Psi}_i) d\tilde{x}d\tilde{y} = I^{\text{orth}}(\hat{x}_0, \hat{y}_0 | \hat{d}) d\hat{x}d\hat{y}, \quad \text{with} \quad d\hat{x}d\hat{y} = \cos \hat{\theta}_i d\tilde{x}d\tilde{y}, \quad (45)$$

where $I^{\text{orth}}(\hat{x}_0, \hat{y}_0 | \hat{d}) d\hat{x}d\hat{y}$ denotes the fraction of power collected on the infinitesimally small surface element $d\hat{x}d\hat{y}$ around point (\hat{x}_0, \hat{y}_0) on P_p with distance \hat{d} from the LS. Therefore, to find $I(\tilde{x}_0, \tilde{y}_0 | \tilde{d}, \hat{\Psi}_i)$ in terms of the known function $I^{\text{orth}}(\hat{x}_0, \hat{y}_0 | \hat{d})$, we need to express (\hat{x}_0, \hat{y}_0) as a function of $(\tilde{x}_0, \tilde{y}_0)$.

We note that P_p lies in the $\hat{x} - \hat{y}$ plane, passes through point $(\tilde{x}_0, \tilde{y}_0)$, which is identical to point (\hat{x}_0, \hat{y}_0) , and its normal vector points in the opposite direction of the incident beam, i.e., $(-\sin \hat{\theta}_i \cos \hat{\phi}_i, -\sin \hat{\theta}_i \sin \hat{\phi}_i, -\cos \hat{\theta}_i)$. We choose the \hat{x} and \hat{y} axes on P_p as follows. First, we choose \hat{y} as the intersection of P_p and P_{np} . Their intersection is given by $\tilde{y} = -\cot \hat{\phi}_i(\tilde{x} - \tilde{x}_0) + \tilde{y}_0$ in the $\tilde{x}\tilde{y}\tilde{z}$ -coordinate system. The line orthogonal to \hat{y} in P_{np} is given by $\tilde{y} = \tan \hat{\phi}_i(\tilde{x} - \tilde{x}_0) + \tilde{y}_0$, which we refer to as line $\hat{\hat{x}}$, and the line orthogonal to \hat{y} in P_p is \hat{x} . As can be seen from the equation defining $\hat{\hat{x}}$, its angle with the \tilde{x} axis is $\hat{\phi}_i$. Moreover, the angle between $\hat{\hat{x}}$ and \hat{x} is $\hat{\theta}_i$. Therefore, the $\hat{x}\hat{y}\hat{z}$ -coordinate system is determined by moving the origin to the beam footprint center on P_p and rotating the axes first around the \tilde{z} axis by angle $\hat{\phi}_i$ counter-clockwise and then rotate them around the resulting new \tilde{y} axis by angle $\hat{\theta}_i$ counter-clockwise. In other words, point $\tilde{\mathbf{a}} = (\tilde{x}_0, \tilde{y}_0)^\top$ in the $\tilde{x}\tilde{y}\tilde{z}$ -coordinate system on P_{np} has coordinates $\hat{\mathbf{a}} = (\hat{x}_0, \hat{y}_0)^\top$ in the $\hat{x}\hat{y}\hat{z}$ -coordinate system on P_p given by $\hat{\mathbf{a}} = \mathbf{T}_{\hat{\theta}_i} \mathbf{R}_{-\hat{\phi}_i} \tilde{\mathbf{a}}$. Substituting this into (45) and noting that $\hat{d} \approx \tilde{d}$ holds for $\tilde{d} \gg \sqrt{\tilde{x}_0^2 + \tilde{y}_0^2}$ leads to (44) and completes the proof of Lemma 6. \blacksquare

Substituting $\hat{\Psi}_i = (\theta_i, 0)$ and (4) into Lemma 6 leads to (21) and completes the proof of Lemma 4.

APPENDIX E

Using Lemma 6 and (24), the left-hand side of (25) is obtained as

$$I_{AG}^{\text{irs}}(x, y | d_{sr}, \hat{\Psi}_i, \hat{\mathbf{w}}_0, \hat{\varphi}) = I_{AG}^{\text{max}}(d_{sr}, \mathbf{w}_0) \cos \hat{\theta}_i \exp(-2\mathbf{a}^\top \mathbf{R}_{-\hat{\phi}_i}^\top \mathbf{T}_{\hat{\theta}_i}^\top \mathbf{R}_{\hat{\varphi}}^\top \mathbf{S}_{\hat{\mathbf{w}}_0}^{d_{sr}} \mathbf{R}_{\hat{\varphi}} \mathbf{T}_{\hat{\theta}_i} \mathbf{R}_{-\hat{\phi}_i} \mathbf{a}), \quad (46)$$

where $\mathbf{a} = (x, y)^\top$ and $\mathbf{S}_{\hat{\mathbf{w}}_0}^{d_{sr}} = \text{diag}\left\{\frac{1}{w^2(d_{sr}, \hat{w}_{01})}, \frac{1}{w^2(d_{sr}, \hat{w}_{02})}\right\}$. Equating (46) and (21), we obtain

$$\mathbf{R}_{-\hat{\phi}_i}^\top \mathbf{T}_{\hat{\theta}_i}^\top \mathbf{R}_{\hat{\varphi}}^\top \mathbf{S}_{\hat{\mathbf{w}}_0}^{d_{sr}} \mathbf{R}_{\hat{\varphi}} \mathbf{T}_{\hat{\theta}_i} \mathbf{R}_{-\hat{\phi}_i} = \mathbf{S}_{\mathbf{w}_0}^{d_{sr}} \mathbf{T}_{\theta_i}^2 \implies \mathbf{R}_{\hat{\varphi}}^\top \mathbf{S}_{\hat{\mathbf{w}}_0}^{d_{sr}} \mathbf{R}_{\hat{\varphi}} = \mathbf{A}. \quad (47)$$

Here, $\mathbf{A} = \mathbf{T}_{\hat{\theta}_i}^{-\top} \mathbf{R}_{-\hat{\phi}_i}^{-\top} \mathbf{S}_{\hat{\mathbf{w}}_0}^{d_{sr}} \mathbf{T}_{\hat{\theta}_i}^2 \mathbf{R}_{-\hat{\phi}_i}^{-1} \mathbf{T}_{\hat{\theta}_i}^{-1} \stackrel{(a)}{=} \mathbf{T}_{\hat{\theta}_i}^{-\top} \mathbf{R}_{\hat{\varphi}}^\top \mathbf{S}_{\hat{\mathbf{w}}_0}^{d_{sr}} \mathbf{T}_{\hat{\theta}_i}^2 \mathbf{R}_{\hat{\varphi}} \mathbf{T}_{\hat{\theta}_i}^{-1}$, where equality (a) follows from $\mathbf{R}_\tau^{-1} = \mathbf{R}_{-\tau}$. Now, we have to find $\hat{\mathbf{w}}_0$ and $\hat{\varphi}$ such that (47) holds. In particular, since the columns of $\mathbf{R}_{\hat{\varphi}}$ are orthonormal and $\mathbf{S}_{\hat{\mathbf{w}}_0}^{d_{sr}}$ is a diagonal matrix, it is in the form of an eigenvalue decomposition. Therefore, the diagonal elements of $\mathbf{S}_{\hat{\mathbf{w}}_0}^{d_{sr}}$ are the eigenvalues of \mathbf{A} and the columns of $\mathbf{R}_{\hat{\varphi}}^\top$ are the corresponding eigenvectors. Finally, we note that for the power distributions in (46) and (21), when the arguments of the exponential functions become identical, the factors multiplied with them become identical as well. This completes the proof.

APPENDIX F

By substituting $\hat{\Psi}_i = (\theta_{rl}, 0)$ and $d = d_{e2e}$ in Lemma 6 and (24), we derive the power density across the lens at point $\mathbf{a} = (x, y)^T$ as follows

$$\begin{aligned} I_{AG}^{\text{lens}}(x, y | d_{e2e}, \hat{\Psi}_i, \hat{\mathbf{w}}_0, \hat{\varphi}) &= \cos \theta_{rl} I_{AG}^{\text{max}}(d_{e2e}, \hat{\mathbf{w}}_0) \exp(-2\mathbf{a}^T \mathbf{B} \mathbf{a}) \\ &\stackrel{(a)}{=} \cos \theta_{rl} I_{AG}^{\text{max}}(d_{e2e}, \hat{\mathbf{w}}_0) \exp(-2\mathbf{d}^T \mathbf{\Lambda} \mathbf{d}), \end{aligned} \quad (48)$$

where $\mathbf{B} = \mathbf{T}_{\theta_{rl}}^T \mathbf{R}_{\hat{\varphi}}^T \mathbf{S}_{\hat{\mathbf{w}}_0}^{d_{e2e}} \mathbf{R}_{\hat{\varphi}} \mathbf{T}_{\theta_{rl}}$. Equality (a) follows from the eigenvalue decomposition of \mathbf{B} , where we have $\mathbf{d} = \mathbf{U}^T \mathbf{a}$. Moreover, \mathbf{U} contains the eigenvectors of \mathbf{B} as its columns and $\mathbf{\Lambda}$ is a diagonal matrix with the corresponding eigenvalues on its main diagonal. Integration of (48) over the lens area yields the power collected by the PD, which can be calculated using the same technique as in [32, Eq. (13) and Appendix C]. This results in (27) and completes the proof.

REFERENCES

- [1] M. Najafi and R. Schober, "Intelligent Reflecting Surfaces for Free Space Optical Communications," in *Proc. IEEE Global Commun. Conf.*, 2019, pp. 1–7.
- [2] M. Khalighi and M. Uysal, "Survey on Free Space Optical Communication: A Communication Theory Perspective," *IEEE Commun. Surveys Tutorials*, vol. 16, no. 4, pp. 2231–2258, 2014.
- [3] A. A. Farid and S. Hranilovic, "Outage Capacity Optimization for Free-Space Optical Links with Pointing Errors," *J. Lightw. Technol.*, vol. 25, no. 7, pp. 1702–1710, Jul. 2007.
- [4] E. J. Lee and V. W. Chan, "Part 1: Optical Communication Over the Clear Turbulent Atmospheric Channel Using Diversity," *IEEE J. Sel. Areas Commun.*, vol. 22, no. 9, pp. 1896–1906, Nov. 2004.
- [5] T. A. Tsiftsis, H. G. Sandalidis, G. K. Karagiannidis, and M. Uysal, "Optical Wireless Links with Spatial Diversity Over Strong Atmospheric Turbulence Channels," *IEEE Trans. Wireless Commun.*, vol. 8, no. 2, pp. 951–957, Feb. 2009.
- [6] M. Khalighi, N. Schwartz, N. Aitamer, and S. Bourennane, "Fading Reduction by Aperture Averaging and Spatial Diversity in Optical Wireless Systems," *IEEE/OSA J. Opt. Commun. Net.*, vol. 1, no. 6, pp. 580–593, 2009.
- [7] R. K. Tyson, "Bit-Error Rate for Free-Space Adaptive Optics Laser Communications," *JOSA A*, vol. 19, no. 4, pp. 753–758, 2002.
- [8] V. Jamali, D. S. Michalopoulos, M. Uysal, and R. Schober, "Link Allocation for Multiuser Systems with Hybrid RF/FSO Backhaul: Delay-Limited and Delay-Tolerant Designs," *IEEE Trans. Wireless Commun.*, vol. 15, no. 5, pp. 3281–3295, May 2016.
- [9] M. Najafi, V. Jamali, D. W. K. Ng, and R. Schober, "C-RAN With Hybrid RF/FSO Fronthaul Links: Joint Optimization of Fronthaul Compression and RF Time Allocation," *IEEE Trans. Commun.*, vol. 67, no. 12, pp. 8678–8695, 2019.
- [10] R. Li, T. Chen, L. Fan, and A. Dang, "Performance Analysis of a Multiuser Dual-Hop Amplify-and-Forward Relay System With FSO/RF Links," *IEEE/OSA J. Opt. Commun. Net.*, vol. 11, no. 7, pp. 362–370, 2019.
- [11] M. Najafi, V. Jamali, and R. Schober, "Optimal Relay Selection for the Parallel Hybrid RF/FSO Relay Channel: Non-Buffer-Aided and Buffer-Aided Designs," *IEEE Trans. Commun.*, vol. 65, no. 7, pp. 2794–2810, Jul. 2017.
- [12] N. Yu, P. Genevet, M. A. Kats, F. Aieta, J.-P. Tetienne, F. Capasso, and Z. Gaburro, "Light Propagation with Phase Discontinuities: Generalized Laws of Reflection and Refraction," *Science*, vol. 334, no. 6054, pp. 333–337, Oct. 2011.
- [13] F. Aieta, P. Genevet, N. Yu, M. A. Kats, Z. Gaburro, and F. Capasso, "Out-of-Plane Reflection and Refraction of Light by Anisotropic Optical Antenna Metasurfaces with Phase Discontinuities," *Nano Letters*, vol. 27, no. 3, pp. 1702–1706, Feb. 2012.

- [14] M. Najafi, V. Jamali, R. Schober, and V. H. Poor, "Physics-based Modeling and Scalable Optimization of Large Intelligent Reflecting Surfaces," Apr. 2020. [Online]. Available: <http://arxiv.org/abs/2004.12957>
- [15] B. Liu, K. Song, , and J. Xiao, "Two-Dimensional Optical Metasurfaces: From Plasmons to Dielectrics," *Advances in Condensed Matter Physics*, vol. 7, 2019. [Online]. Available: <https://doi.org/10.1155/2019/2329168>
- [16] Y.-W. Huang, H. W. H. Lee, R. Sokhoyan, R. A. Pala, K. Thyagarajan, S. Han, D. P. Tsai, and H. A. Atwater, "Gate-Tunable Conducting Oxide Metasurfaces," *Nano Lett.*, vol. 16, no. 9, pp. 5319–5325, 2016.
- [17] X. Luo, "Subwavelength Artificial Structures: Opening a New Era for Engineering Optics," *Advanced Materials*, vol. 31, no. 4, p. 1804680, 2019.
- [18] A. Nemati, Q. Wang, M. Hong, and J. Teng, "Tunable and Reconfigurable Metasurfaces and Metadevices," *Opto-Electronic Advances*, vol. 1, no. 5, p. 180009, 2018.
- [19] S. M. Choudhury, D. Wang, K. Chaudhuri, C. DeVault, A. V. Kildishev, A. Boltasseva, and V. M. Shalaev, "Material Platforms for Optical Metasurfaces," *Nanophotonics*, vol. 7, no. 6, pp. 959–987, 2018.
- [20] A. E. Minovich, A. E. Miroshnichenko, A. Y. Bykov, T. V. Murzina, D. N. Neshev, and Y. S. Kivshar, "Functional and Nonlinear Optical Metasurfaces," *Laser & Photonics Reviews*, vol. 9, no. 2, pp. 195–213, 2015.
- [21] L. Zou, M. Cryan, and M. Klemm, "Phase Change Material Based Tunable Reflectarray for Free-Space Optical Inter/Intra Chip Interconnects," *Opt. Express*, vol. 22, no. 20, pp. 24 142–24 148, Oct. 2014.
- [22] Z. Cao, X. Zhang, G. Osnabrugge, J. Li, I. M. Vellekoop, and A. M. Koonen, "Reconfigurable Beam System for Non-Line-of-Sight Free-Space Optical Communication," *Light: Science & Applications*, vol. 8, no. 1, pp. 1–9, 2019.
- [23] C. Valagiannopoulos, T. A. Tsiftsis, and V. Kovanis, "Metasurface-enabled Interference Mitigation in Visible Light Communication Architectures," *Journal of Optics*, vol. 21, no. 11, p. 115702, 2019.
- [24] A. M. A. Abdelhady, A. S. Salem, O. Amin, B. Shihada, and M.-S. Alouini, "VLC via Intelligent Reflecting Surfaces: Metasurfaces vs Mirror Arrays," 2020. [Online]. Available: <http://hdl.handle.net/10754/661379>
- [25] K. Park, H. M. Oubei, W. G. Alheadary, B. S. Ooi, and M. Alouini, "A Novel Mirror-Aided Non-Imaging Receiver for Indoor 2×2 MIMO-Visible Light Communication Systems," *IEEE Trans. Wireless Commun.*, vol. 16, no. 9, pp. 5630–5643, Sept. 2017.
- [26] J. W. Goodman, *Introduction to Fourier Optics*. Roberts and Company Publishers, 2005.
- [27] B. Ratni, A. de Lustrac, G.-P. Piau, and S. N. Burokur, "Reconfigurable Meta-Mirror for Wavefronts Control: Applications to Microwave Antennas," *Opt. Express*, vol. 26, no. 3, pp. 2613–2624, Feb. 2018.
- [28] E. Kochkina, G. Wanner, D. Schmelzer, M. Tröbs, and G. Heinzel, "Modeling of the General Astigmatic Gaussian Beam and its Propagation Through 3D Optical Systems," *Appl. Opt.*, vol. 52, no. 24, pp. 6030–6040, Aug. 2013.
- [29] N. M. Estakhri and A. Alù, "Wave-front Transformation with Gradient Metasurfaces," *Physical Review X*, vol. 6, no. 4, p. 041008, 2016.
- [30] R. A. Serway and J. W. Jewett, *Physics for Scientists and Engineers with Modern Physics*. Cengage learning, 2018.
- [31] S. Huang and M. Safari, "Free-Space Optical Communication Impaired by Angular Fluctuations," *IEEE Trans. Wireless Commun.*, vol. 16, no. 11, pp. 7475–7487, Nov. 2017.
- [32] M. Najafi, H. Ajam, V. Jamali, P. D. Diamantoulakis, G. K. Karagiannidis, and R. Schober, "Statistical Modeling of the FSO Fronthaul Channel for UAV-based Communications," *IEEE Trans. Commun.*, pp. 1–1, 2020.
- [33] H. AlQuwaiee, H. C. Yang, and M. S. Alouini, "On the Asymptotic Capacity of Dual-Aperture FSO Systems with Generalized Pointing Error Model," *IEEE Trans. Wireless Commun.*, vol. 15, no. 9, pp. 6502–6512, Sept. 2016.
- [34] I. S. Gradshteyn and I. M. Ryzhik, *Table of Integrals, Series, and Products*. 7th ed. Academic, 2007.